Inversion of Large-Support Ill-Posed Linear Operators Using a Piecewise Gaussian MRF

Mila Nikolova, Jérôme Idier, and Ali Mohammad-Djafari, *Member, IEEE*

***Abstract*—We propose a method for the reconstruction of signals and images observed *partially* through a linear operator with a *large support* (e.g., a Fourier transform on a sparse set). This inverse problem is ill-posed and we resolve it by incorporating the prior information that the reconstructed objects are composed of smooth regions separated by sharp transitions. This feature is modeled by a *piecewise Gaussian* (PG) *Markov random field* (MRF), known also as the *weak-string* in one dimension and the *weak-membrane* in two dimensions. The reconstruction is defined as the maximum *a posteriori* estimate.**

The prerequisite for the use of such a prior is the success of the optimization stage. The posterior energy corresponding to a PG MRF is generally *multimodal* and its minimization is particularly problematic. In this context, general forms of simulated annealing rapidly become intractable when the observation operator extends over a large support.

In this paper, global optimization is dealt with by extending the *graduated nonconvexity* (GNC) algorithm to ill-posed linear inverse problems. GNC has been pioneered by Blake and Zisserman in the field of image segmentation. The resulting algorithm is mathematically suboptimal but it is seen to be very efficient in practice. We show that the original GNC does not correctly apply to ill-posed problems. Our extension is based on a proper theoretical analysis, which provides further insight into the GNC. The performance of the proposed algorithm is corroborated by a synthetic example in the area of diffraction tomography.

***Index Terms*— Discontinuity recovery, GNC optimization, ill-posed inverse problems, image reconstruction, MAP estimation, MRF modeling, tomography.**

I. Introduction

A. Background

MANY physical experiments seek to map a real-valued object from only partial observation through an imperfect measurement device. For our purposes, we consider the very common case of a signal or an image $\boldsymbol{x}$ (called *object* in the following), observed through a linear operator $\mathcal{A}$, when additive white Gaussian noise $\boldsymbol{n} \sim \mathcal{N}(\mathbf{0}, \sigma^2 I)$ accounts for uncertainties (I stands for the identity operator). The discrete form of such an observation model is

$$\boldsymbol{y} = \mathcal{A}\boldsymbol{x} + \boldsymbol{n} = \sum_{i=1}^{M} \boldsymbol{a}_i x_i + \boldsymbol{n}. \tag{1}$$

The unknown object $\boldsymbol{x} = [x_1, \cdots, x_M]^T \in \mathbb{R}^M$ is defined on an M-point lattice $\mathcal{S}$, either one-dimensional (1-D) or two-dimensional (2-D). Data $\boldsymbol{y} \in \mathbb{R}^N$ are assumed real for sake of clarity; adaptation to the complex case is straightforward.

More specifically, our main concern will be to deal with the conjunction of the following two acknowledged difficulties concerning the observation operator $\mathcal{A} = [\boldsymbol{a}_1, \cdots, \boldsymbol{a}_M] \in \mathbb{R}^{N \times M}$.

(A1) $\mathcal{A}$ originates from an ill-posed continuous equation, so it is either *ill-conditioned*, or *singular* with $M > N$, or both.

(A2) $\mathcal{A}$ is *not sparse*, i.e., its *support*, defined as $\text{supp}(\mathcal{A}) = \{(i, j);\ \mathcal{A}_{i,j} \neq 0\}$, is *large*: each datum y_j results from the contribution of many elements of the object, even the entire object. In fact, under the Gaussian observation model (1), it appears that $\text{supp}(\mathcal{A}^T\mathcal{A})$ plays the essential role in the definition of posterior contributions, rather than $\text{supp}(\mathcal{A})$ (see Section III).

Such a conjunction is a major practical issue for image reconstruction, and also in many areas such as X-ray or diffraction tomography (see Section VIII) [11], [21], [26], radio-interferometry, synthetic aperture radar, geophysics [24], [33], nondestructive evaluation [40], etc. Most of the observation operators involved in these applications present no special structure favorable to be exploited numerically.

The *reconstruction* of $\boldsymbol{x}$ from $\boldsymbol{y}$ is an *ill-posed* inverse problem [10], [37]. Its resolution relies on *prior information* about $\boldsymbol{x}$. An important class of real-world objects are composed of nearly homogeneous regions separated by edges: such are the objects we are seeking to reconstruct. The pioneering work of Geman and Geman [18] shows that such objects may be well described by *coupled* Markov random fields (MRF's). The object is modeled as a random pair $(\boldsymbol{x}, \boldsymbol{\ell})$ consisting of an *intensity process* $\boldsymbol{x}$ and an unobservable process $\boldsymbol{\ell}$ of *line* or *label* variables. Prior knowledge about $\boldsymbol{x}$ is conveyed by a coupled probability distribution $P(\boldsymbol{x}, \boldsymbol{\ell}) = (1/Z)\exp[-\Psi(\boldsymbol{x}, \boldsymbol{\ell})]$, where Ψ is the coupled prior energy of $\boldsymbol{x}$ and Z is the partition function. Among several reasonable choices [2], the optimal reconstruction $(\hat{\boldsymbol{x}}, \hat{\boldsymbol{\ell}})$ is defined as the maximizer of the posterior distribution $P(\boldsymbol{x}, \boldsymbol{\ell}|\boldsymbol{y})$ or, equivalently, as the minimizer of the posterior

Manuscript received January 8, 1996; revised April 3, 1997. Portions of this work were presented at the 1994 IEEE ICASSP, Adelaide, Australia. The associate editor coordinating the review of this manuscript and approving it for publication was Prof. Andrew Yagle.

The authors are with the Laboratoire des Signaux et Systèmes (CNRS–ESE–UPS), Supélec, Plateau de Moulon, 91192 Gif-sur-Yvette Cedex, France (e-mail: nikolova@lss.supelec.fr).

Publisher Item Identifier S 1057-7149(98)02463-4.

energy $E(\boldsymbol{x}, \boldsymbol{\ell}) = \|\mathcal{A}\boldsymbol{x} - \boldsymbol{y}\|^2 + \Psi(\boldsymbol{x}, \boldsymbol{\ell})$. The first term—the negative log-likelihood—accounts for *fidelity* to the data and its form steers from the additive white Gaussian nature of the noise, while the second *regularizes* its minimization.

The posterior energy $E(\boldsymbol{x}, \boldsymbol{\ell})$ is nonconvex in $(\boldsymbol{x}, \boldsymbol{\ell})$ and has numerous local minima, so *global* optimization is arduous if not impractical. Provided that $\text{supp}(\mathcal{A}^T\mathcal{A})$ is a reduced set, it can be performed using simulated annealing (SA) stochastic algorithms [18], [25]. Such a situation arises in image segmentation, where $\mathcal{A}$ is diagonal, or in deconvolution problems, when the blur spreads over a small window.

However, general forms of SA are intractable under (A1) and (A2) [19], [39] and *coupled* MRF's have been used only in several *special* cases. In [12], an MRF with a label field is used for the reconstruction of objects with axial symmetry from X-ray tomography data. In this case $\text{supp}(\mathcal{A}^T\mathcal{A})$ is "moderate" ($\text{supp}\,\boldsymbol{a}^j$ is a "line" going through object $\boldsymbol{x}$) and a local minimum is calculated using the iterated conditional modes (ICM) algorithm. Recently, an efficient SA optimization based on the fast Fourier transform (FFT) was developed in the special case when $\mathcal{A}$ is shift-invariant [19] and the line process noninteracting. A deterministic suboptimal initialization-dependent version can be found in [9].

Instead, various methods giving rise to *convex* optimality criteria are used in the context of (A1) and (A2). *Analytic methods* (inverse filtering in signal and image restoration, or backprojection and backpropagation in tomographic reconstruction, etc.), are computationally inexpensive, but they break down in the presence of noise [11], [26]. *Maximum entropy* methods can be very efficient for images with a spiky appearance over a homogeneous background [13], [27]. *Gaussian MRF's* give rise to linear estimators, but the basic homogeneous Gaussian MRF's are well known to allow noise cancellation only at the expense of oversmoothing the object [35], [40]. *Generalized Gaussian (GG) MRF's* [7] preserve edges better while maintaining convex energies. In the same way, other useful MRF's weight the differences between neighbors using a *Huber function* or a *log-cosh* function [20]. A discrepancy measure on neighbors was introduced in [32] in order to model correlations in positive objects. However, none of these priors can give rise to *maximum a posteriori* (MAP) estimators truly accounting for the presence of both homogeneous parts and edges in the object.

In this paper, we focus on pairwise interaction *piecewise Gaussian MRF's* (PG MRF's) with a *noninteracting* Boolean line process $\boldsymbol{\ell}$. This is one of the most common and simple models involving a line process, and it is often used in image processing for the purposes of segmentation, noise cancellation, interpolation [25]. In the field of computer vision, weak strings (in one dimension) and weak membranes (in two dimensions) [4], [8], [15], [29], [36] are widely spread models whose energy can be identified to the negative log-likelihood of PG MRF's. A broader family of PG MRF's with a continuous-valued line process has been introduced by Geman and Reynolds [17]. Given their duality results and following the lines of the present paper, it is realistic to consider that "soft edges" can also be dealt with using GNC. Such an extension is left for future works. A noninteracting line process $\boldsymbol{\ell}$ allows easy determination of $\hat{\boldsymbol{\ell}}(\boldsymbol{x}) = \arg\min_{\boldsymbol{\ell}}[\Psi(\boldsymbol{x}, \boldsymbol{\ell})]$. The MAP estimate $\hat{\boldsymbol{x}}$ also minimizes the energy $\mathcal{E}(\boldsymbol{x}) = \|\mathcal{A}\boldsymbol{x} - \boldsymbol{y}\|^2 + \Phi(\boldsymbol{x})$, where $\Phi(\boldsymbol{x}) = \Psi[\boldsymbol{x}, \hat{\boldsymbol{\ell}}(\boldsymbol{x})]$ is a truncated quadratic function if $\boldsymbol{\ell}$ is Boolean.

Our motivation to use this model is not only due to its qualities, but also to the fact that an appealing algorithm is available for the minimization of $\mathcal{E}(\boldsymbol{x})$ when $\mathcal{A} = I$: the *graduated nonconvexity algorithm* (GNC), which was proposed by Blake and Zisserman [4]. It is based on minimum tracking by local descent along a family of *relaxed* energies, the first of which is *convex* and the final is $\mathcal{E}(\boldsymbol{x})$. It is a suboptimal but practically very efficient algorithm.

B. Content of the Paper

Our paper provides an extension and a deepening of the whole estimation-optimization approach developed by Blake and Zisserman, in order to cope with (A1) and (A2). The PG MRF is briefly presented in Section II. The MAP estimator reads equivalently as the minimizer of the energy of intensities $\mathcal{E}(\boldsymbol{x})$ only which is *multimodal*. The ability of various global optimization techniques to cope with (A1) and (A2) is analyzed in Section III.

The *original* GNC—as pioneered in [4] for the case $\mathcal{A} = I$—is presented in Section IV. Its extension to arbitrary $\mathcal{A}$ needs further analysis and the relevant theoretical developments are given in Section V. Extending this GNC to arbitrary well-conditioned observation operators $\mathcal{A}$ is straightforward. Such is not the case when $\mathcal{A}$ is ill conditioned or singular—the main difference concerns the obtaining of an initial convex energy, in which case we propose a *doubly* relaxed GNC (Section VI). Several results concerning the evolution of the solution are stated in Section VII. A criterion to recognize the *ultimate* GNC solution is established and a simple stopping rule is deduced. On the other hand, both solution and relaxation are closely linked to the *scale* of $\mathcal{A}$. General recommendations about the relaxation are then presented.

By way of application, we present a *diffraction tomography* synthetic example. Reconstruction results obtained using various convex prior energies are compared to those obtained using a PG MRF (Section VIII). Concluding remarks are given in Section IX. Most of the proofs of the theorems and lemmas in the paper are presented in the Appendix.

II. Piecewise Gaussian Model and MAP Estimation

A. Coupled Prior

In the following, theory is formulated in 2-D for the four nearest-neighbor case but its extension to other configurations such as the 2-D eight nearest-neighbor case, 1-D signals and three-dimensional (3-D) objects is straightforward. Let $\mathcal{S} = \{\mathcal{S}_i, i = 1, \cdots, M\}$ be the integer grid corresponding to the set of the sites of $\boldsymbol{x}$. We consider the four nearest-neighborhood system $\mathcal{N}$ corresponding to the set of *maximal* second-order cliques $\mathcal{C}$: no maximal clique is a subset of a strictly larger clique, so $\mathcal{C} = \{(i, j)/\|\mathcal{S}_i - \mathcal{S}_j\|_2^2 = 1\}$. A binary 0-1 line variable $\ell_{i,j}$ is associated with each maximal clique $\{i, j\} \in \mathcal{C}$, in order to control its bonding strength. The

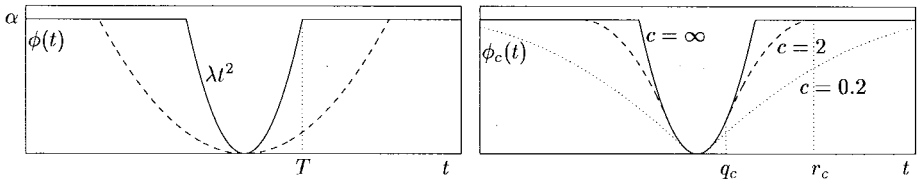

(a) (b)

Fig. 1. (a) Truncated quadratic function $\phi(t)$ as defined in (4) for $(\alpha, \lambda) = (1, 0.6)$ (- -) and $(\alpha, \lambda) = (1, 1.5)$ (—). (b) Relaxation of the truncated quadratic function $\phi_c(t)$ given in (10): $c = 0.2$ (:), $c = 2$ (- -) and $c = \infty$ (—).

coupled prior energy $\Psi_{\tilde{\alpha},\tilde{\lambda}}$ only involves the set of *transitions* $\{t_{i,j} = x_i - x_j/(i,j) \in \mathcal{C}\}$ and the corresponding $\ell_{i,j}$s [4], [18], as follows:

$$\Psi_{\tilde{\alpha},\tilde{\lambda}}(\boldsymbol{x}, \boldsymbol{\ell}) = \sum_{\{i,j\}\in\mathcal{C}} \psi_{\tilde{\alpha},\tilde{\lambda}}(t_{i,j}, \ell_{i,j}),$$
$$\psi_{\tilde{\alpha},\tilde{\lambda}}(t, \ell) = \tilde{\lambda}^2 t^2 (1-\ell) + \tilde{\alpha}\ell,$$

where $\psi_{\tilde{\alpha},\tilde{\lambda}}$ is a *potential* function and $(\tilde{\alpha}, \tilde{\lambda})$ are positive parameters.

Remark 1: Prior energy $\Psi_{\tilde{\alpha},\tilde{\lambda}}$ does not derive from a normalized probability measure on $\boldsymbol{x}$ in $\mathbb{R}^M$, because the partition function

$$\begin{aligned} Z_X &= \int \sum_{\boldsymbol{\ell}} e^{-\Psi_{\tilde{\alpha},\tilde{\lambda}}(\boldsymbol{x},\boldsymbol{\ell})}\, d\boldsymbol{x} \\ &= \int \prod_{\{i,j\}\in\mathcal{C}} \sum_{\ell_{i,j}\in\{0,1\}} e^{-\psi_{\tilde{\alpha},\tilde{\lambda}}(t_{i,j},\ell_{i,j})}\, d\boldsymbol{x} \\ &= \int \prod_{\{i,j\}\in\mathcal{C}} (e^{-\tilde{\lambda}^2 t_{i,j}^2} + e^{-\tilde{\alpha}})\, d\boldsymbol{x} \end{aligned}$$

is finite only for $\boldsymbol{x}$ belonging to a *bounded* set in $\mathbb{R}^M$. Nevertheless, the *a posteriori* measure is a proper probability measure provided that $\mathcal{A}^T\mathcal{A}$ is invertible. Otherwise, a further examination may be necessary in order to verify whether the MAP estimate is well defined. For instance, the *a posteriori* measure is improper and the MAP solution is only defined up to an arbitrary constant level when $\mathcal{A}\mathbf{1} = \mathbf{0}$ ($\mathbf{1} \in \mathbb{R}^M$, $\mathbf{1} = [1, \cdots, 1]^T$).

B. Optimal MAP Solution

The optimal solution pair $(\hat{\boldsymbol{x}}, \hat{\boldsymbol{\ell}})$ is defined as the minimizer of

$$E(\boldsymbol{x}, \boldsymbol{\ell}) = \|\mathcal{A}\boldsymbol{x} - \boldsymbol{y}\|^2 + \Psi_{\alpha,\lambda}(\boldsymbol{x}, \boldsymbol{\ell})$$

where $\alpha = 2\sigma^2\tilde{\alpha}$ and $\lambda = \sqrt{2}\sigma\tilde{\lambda}$, so that we have $\Psi_{\alpha,\lambda}(\boldsymbol{x}, \boldsymbol{\ell}) = 2\sigma^2\Psi_{\tilde{\alpha},\tilde{\lambda}}(\boldsymbol{x}, \boldsymbol{\ell})$. In the following, $\Psi_{\alpha,\lambda}$ and $\psi_{\alpha,\lambda}$ are denoted Ψ and ψ. The model parameters (α, λ) play a crucial role for the quality of the estimation. As regards their selection, a detailed study is presented in [4] when $\mathcal{A} = I$. When $\mathcal{A} \neq I$, a numerical method is proposed in [30] for 1-D signals. We do not discuss this question in the present paper.

Because the line variables are noninteracting, for each $\boldsymbol{x}$ *fixed*, the optimal line process $\hat{\boldsymbol{\ell}}(\boldsymbol{x}) = \arg\min_{\boldsymbol{\ell}} E(\boldsymbol{x}, \boldsymbol{\ell})$ reduces to minimization of each $\psi(t_{ij}, \ell_{i,j})$ *separately* w.r.t. $\ell_{i,j}$ [4]:

$$\begin{aligned} \hat{\ell}(t) &= \arg\min_{\ell\in\{0,1\}} \psi(t, \ell) \\ &= 1 - \mathbb{1}(|t| < T), \qquad T = \frac{\sqrt{\alpha}}{\lambda} \end{aligned} \tag{2}$$

where $\mathbb{1}$ means indicator function: $\mathbb{1}(|t| < T) = 1$ if $|t| < T$ and $\mathbb{1}(|t| < T) = 0$, otherwise. Knowing $\hat{\ell}$ is equivalent to knowing whether $|t| < T$ (pixels belong to the same homogeneous zone) or $|t| \geq T$ (an edge separates them). Each transition t can be *classified* as

$$\begin{cases} \text{continuous}, & \text{if } |t| < T, \\ \text{discontinuous}, & \text{if } |t| \geq T. \end{cases} \tag{3}$$

The line variables can be eliminated from the expression of the MAP estimator

$$\phi(t) = \psi[t, \hat{\ell}(t)] = \lambda^2 t^2 \mathbb{1}(|t| < T) + \alpha\mathbb{1}(|t| \geq T), \tag{4}$$
$$\Phi(\boldsymbol{x}) = \Psi[\boldsymbol{x}, \hat{\boldsymbol{\ell}}(\boldsymbol{x})] = \sum_{\{i,j\}\in\mathcal{C}} \phi(t_{i,j}), \tag{5}$$
$$\mathcal{E}(\boldsymbol{x}) = E[\boldsymbol{x}, \hat{\boldsymbol{\ell}}(\boldsymbol{x})] = \|\mathcal{A}\boldsymbol{x} - \boldsymbol{y}\|^2 + \Phi(\boldsymbol{x}). \tag{6}$$

The resultant potential function $\phi(t)$ in (4) is shown in Fig. 1(a). The MAP energy $\mathcal{E}(\boldsymbol{x})$ depends on the intensity process $\boldsymbol{x}$ only, although its minimizer $\hat{\boldsymbol{x}} = \arg\min_{\boldsymbol{x}} \mathcal{E}(\boldsymbol{x})$ yields the optimal line process $\hat{\boldsymbol{\ell}}(\hat{\boldsymbol{x}})$ using (2).

III. Optimization Challenge

The posterior energy $\mathcal{E}(\boldsymbol{x})$ (6) generally exhibits many local minima and the calculation of the global minimum $\hat{\boldsymbol{x}}$ is a difficult optimization task. It is often encountered in image processing where different techniques, either stochastic or deterministic, are developed. In this section, such methods are briefly reviewed and possible extensions are discussed.

A. Posterior Neighborhood and Simulated Annealing

Since [18], the most popular algorithm for the minimization of MRF posterior energies remains *simulated annealing*: it is a stochastic algorithm, providing asymptotic weak convergence toward the set of the global minima. Let $\{\tau_k, k = 0, 1, \cdots\}$ be a sequence of temperatures, decreasing from an initial high value to zero. To each temperature τ is associated a Gibbs measure $p_\tau(\boldsymbol{x}|\boldsymbol{y}) \propto \exp[-\mathcal{E}(\boldsymbol{x})/\tau]$. Let $(i_k)_{k\geq 1}$ be the sequence of visits of the sites of $\mathcal{S}$. At the kth step, $\tau = \tau_k$ and the object $\boldsymbol{x}^{(k)}$ is obtained from $\boldsymbol{x}^{(k-1)}$ by updating only the

element i to the value ξ which is obtained from the posterior conditional distribution using Gibbs sampling [18], as follows:

$$p_\tau[X_i = \xi | x_j^{(k-1)},\, j \in \mathcal{S} \setminus \{i\},\, \boldsymbol{y}] = p_\tau[X_i = \xi | x_j^{(k-1)},\, j \in \mathcal{N}_i^P,\, \boldsymbol{y}]. \quad (7)$$

In order to perform a general form of such a SA optimization, it is necessary to determine the structure of the posterior neighborhood $\mathcal{N}^P$. Each $\mathcal{N}_i^P$ depends jointly on $\mathcal{N}_i$ and on the support of $\mathcal{A}$. In [18], this link has been established for operators which can be linear or nonlinear but with a shift-invariant symmetric support (typically, when $\mathcal{A}$ represents a blur kernel). For linear operators with *irregular* supports, the following theorem states a general formula with no restriction on $\mathcal{A}$; its proof is given in the Appendix.

Theorem 1—Posterior Neighborhood: Let $\mathcal{N}_i$ be the neighbors of i in the prior; then the set $\mathcal{N}_i^P$ of neighbors of i in the posterior distribution $p(\boldsymbol{x}|\boldsymbol{y})$ is given by

$$\begin{aligned}\mathcal{N}_i^P &= \mathcal{N}_i^{\mathcal{A}} \cup \mathcal{N}_i,\\ \mathcal{N}_i^{\mathcal{A}} &= \{j \in \mathcal{S} \setminus \{i\} \text{ such that } \boldsymbol{a}_i^T \boldsymbol{a}_j \neq 0\}\\ &= \{j \in \mathcal{S} \setminus \{i\} \text{ such that } \{i, j\} \in \text{supp}(\mathcal{A}^T\mathcal{A})\}\end{aligned}$$

where $\mathcal{N}_i^{\mathcal{A}}$ is the set of the neighbors of i due to $\mathcal{A}$.

Numerical efficiency of standard SA directly depends on the evaluation cost of (7) and hence on the size of $\mathcal{N}^P$. Recently, a new implementation of SA has been proposed for shift-invariant observation operators and Markovian priors with a *noninteracting* line process [19]. It is based on global updates using FFT's rather than on local updates, so that its applicability no more depends on the size of supp$(\mathcal{A}^T\mathcal{A})$. On the other hand, shift invariance yields a specific block-circulant structure for matrix $\mathcal{A}$, and the new SA form is only relevant in this context. Unfortunately, most of the reconstruction problems give rise to spatially variant operators (e.g., when projection arrays do not circularly surround the object). In the example treated in Section VIII, $\mathcal{A}$ is shift-variant and the interactions in the posterior distribution are *global*: $\mathcal{N}_i^P = \mathcal{S}$, $\forall i \in \mathcal{S}$. In such a case, both forms of SA remain intractable.

B. Deterministic Surrogates

Where SA proves to be too costly, several deterministic suboptimal strategies have been proposed. Let us examine the main possibilities available for PG MRF's.

Iterated conditional modes (ICM) [1] locally maximizes $p(\boldsymbol{x}|\boldsymbol{y})$ by iterative maximization of (7), but the solution strongly depends on initialization and scanning order.

Multiresolution or multigrid decompositions can partly cope the problem, since it is expected that MAP energies present fewer local minima at coarse scales. So MAP energies are constructed at an increasing scale, and each energy is locally minimized in the vicinity of the previously obtained solution [4], [6].

In [8], a *variational calculus*-based technique for 1-D signals is proposed. Since, for distant edges, optimal points for edge location locally maximize the gradient, an alternating estimation-detection procedure is proposed. It can be very unstable in the presence of noise and close edges, and when $\mathcal{A}$ is ill-conditioned.

On the other hand, several types of methods resort to the *continuation* principle [31], [38]. To our knowledge, all of them have been proposed in the context of a well-posed, *pointwise* observation operator. In the *mean-field annealing* (MFA) framework [3], [15], [16], [34], the line process is replaced by its mean at a varying temperature $\overline{\boldsymbol{\ell}}_T$, so $\Phi_\tau(\boldsymbol{x}) = \Psi(\boldsymbol{x}, \overline{\boldsymbol{\ell}}_\tau)/\tau$. Local minimization of the resulting sequence of approximated energies leads to the MFA solution as a local minimum of $\mathcal{E}$. GNC [4] and *simulated tearing* [14] are more directly built on the *continuation* principle. We focus now on GNC.

IV. Original Graduated Nonconvexity: $\mathcal{A} = I$

Except for additional notation, this section is only a brief summary of [4]. The GNC algorithm was initially proposed by Blake and Zisserman [4] for the global minimization of

$$\mathcal{E}(\boldsymbol{x}) = \|\boldsymbol{x} - \boldsymbol{y}\|^2 + \Phi(\boldsymbol{x}) \quad (8)$$

for the purpose of segmentation or noise cancellation. Global minimization is substituted for a sequence of *local* minimizations (performed by a descent algorithm) of continuously differentiable *relaxed energies* $(\mathcal{E}_{c_k})_{k\geq 0}$ starting from a *convex* relaxed energy $\mathcal{E}_{c_0}(\boldsymbol{x})$ and converging toward the original energy as follows:

$$\lim_{k\to\infty} \mathcal{E}_{c_k}(\boldsymbol{x}) \to \mathcal{E}(\boldsymbol{x}).$$

$c_k > 0$ is the relaxation parameter and $(c_k)_{k\geq 0}$ is an increasing relaxation sequence.

In the following, $\check{\boldsymbol{x}}$ denotes any local minimum while $\hat{\boldsymbol{x}}$ is reserved for global minima. Let $\hat{\boldsymbol{x}}^{(c_0)}$ be the unique minimizer of $\mathcal{E}_{c_0}(\boldsymbol{x})$. For each $k \geq 1$, an *intermediate solution* $\check{\boldsymbol{x}}^{(c_k)}$ is calculated by minimizing $\mathcal{E}_{c_k}(\boldsymbol{x})$ *locally*, starting from the previously obtained $\check{\boldsymbol{x}}^{(c_{k-1})}$:

$$\check{\boldsymbol{x}}^{(c_k)} = \arg \min_{\boldsymbol{x} \in \mathcal{V}[\check{\boldsymbol{x}}^{(c_{k-1})}]} \mathcal{E}_{c_k}(\boldsymbol{x}),$$

where $\mathcal{V}(\boldsymbol{x})$ stands for the attraction valley of $\boldsymbol{x}$.

Whenever unambiguous, we write c for c_k. Since the first term in (8) is already convex and twice continuously differentiable, $\mathcal{E}_c(\boldsymbol{x})$ can be written in the form

$$\begin{aligned}\mathcal{E}_c(\boldsymbol{x}) &= \|\boldsymbol{x} - \boldsymbol{y}\|^2 + \Phi_c(\boldsymbol{x}),\\ \Phi_c(\boldsymbol{x}) &= \sum_{\{i,j\}\in\mathcal{C}} \phi_c(t_{i,j}).\end{aligned} \quad (9)$$

The concavity of the relaxed prior energy $\Phi_c(\boldsymbol{x})$ results from the concavity of each relaxed potential $\phi_c(t)$. The latter can easily be controlled by fitting quadratic splines in the neighborhood of $\pm T$ [see Fig. 1(b)] as follows:

$$\begin{aligned}\phi_c(t) &= \begin{cases}(\lambda t)^2, & \text{if } |t| < q_c,\\ \alpha - \frac{1}{2}c(|t| - r_c)^2, & \text{if } q_c \leq |t| < r_c,\\ \alpha, & \text{if } |t| \geq r_c,\end{cases}\\ q_c &= T(1 + 2\lambda^2/c)^{(-1/2)},\\ r_c &= T(1 + 2\lambda^2/c)^{(1/2)}.\end{aligned} \quad (10)$$

Then $\phi_c''(t) = -c$ for $q_c \leq |t| < r_c$ and $\phi_c''(t) \geq -c, \forall\, t$, so the concavity of $\Phi_c(\boldsymbol{x})$ can be reduced arbitrarily. In this way a new auxiliary state has been introduced into the classification (3), i.e., w.r.t. the relaxation parameter c, a transition t is called

$$\begin{cases} \text{continuous}, & \text{if } |t| < q_c, \\ \textit{undetermined}, & \text{if } q_c \leq |t| < r_c, \\ \text{discontinuous}, & \text{if } |t| \geq r_c. \end{cases} \tag{11}$$

The relaxed energy $\mathcal{E}_c(\boldsymbol{x})$ is convex on $\mathbb{R}^M$ when even the maximum concavity of $\Phi_c(\boldsymbol{x})$ is compensated by the convexity of the data-fidelity term. The value c_0 at which this occurs [$\mathcal{E}(\boldsymbol{x})$ convex for $c < c_0$] can be found by checking whether the Hessian matrix of $\mathcal{E}_c(\boldsymbol{x})$, denoted $\mathcal{E}_c''(\boldsymbol{x})$, is positive definite $\forall\, \boldsymbol{x}$ [22]. From such considerations, Blake and Zisserman [4] are driven to $c_0 = 0.5$ for a signal and $c_0 = 0.25$ for an image, when $\mathcal{A} = I$.

There is no general mathematical proof of convergence of the ultimate GNC solution $\tilde{\boldsymbol{x}}^{(\infty)}$ toward the global minimum $\hat{\boldsymbol{x}}$ for a general nonconvex energy $\mathcal{E}(\boldsymbol{x})$. However, Blake and Zisserman have analytically shown global convergence for important *special* cases. Moreover, its practical convergence in various situations is corroborated numerically [4], [5].

V. General Conditions for Initial Convexity

For an observation operator $\mathcal{A}$ which is no longer identity, application of GNC is not very sensitive to (A2), since it only makes use of standard descent algorithms. On the other hand, conditions for initial convexity of the relaxed energy

$$\mathcal{E}_c(\boldsymbol{x}) = \|\mathcal{A}\boldsymbol{x} - \boldsymbol{y}\|^2 + \Phi_c(\boldsymbol{x}) \tag{12}$$

become more subtle depending on (A1). Whenever $\mathcal{A}^T\mathcal{A}$ is full-rank, $(\mathcal{E}_c)_{c>0}$ admits convex elements. When $\mathcal{A}^T\mathcal{A}$ is singular, the data fidelity term is completely flat in affine subspaces parallel to $\ker(\mathcal{A}^T\mathcal{A})$, so the concavity of $\Phi_c(\boldsymbol{x})$ cannot be compensated.

Let us examine the full-rank case first. The Hessian matrix of $\mathcal{E}_c(\boldsymbol{x})$ at $\boldsymbol{x}$ reads

$$\mathcal{E}_c''(\boldsymbol{x}) = 2\mathcal{A}^T\mathcal{A} + \Phi_c''(\boldsymbol{x}) \tag{13}$$

where $\mathcal{F}''(\boldsymbol{x}) \stackrel{def}{=} \{\partial^2 \mathcal{F}(\boldsymbol{x})/\partial x_i \partial x_j\}$ stands for the Hessian matrix of any term of energy $\mathcal{F}(\boldsymbol{x})$, by a slight abuse of notation. Nonzero entries of $\Phi_c''(\boldsymbol{x})$ read

$$[\Phi_c'']_{i,j} = \begin{cases} -2\lambda^2, & \text{if } |t_{i,j}| < q_c \\ c, & \text{if } q_c \leq |t_{i,j}| < r_c \end{cases}, \text{ if } \{i,j\} \in \mathcal{C} \tag{14}$$

$$[\Phi_c'']_{i,i} = -\sum_{j/\{i,j\}\in\mathcal{C}} [\Phi_c'']_{i,j}, \qquad i = 1, \cdots, M. \tag{15}$$

Let $\mathcal{D}$ be the difference operator which provides the set of transitions involved in $\Phi_c(\boldsymbol{x})$. More precisely, if $\boldsymbol{x}$ is a signal, $\mathcal{D}$ is a $(M-1 \times M)$ Toëplitz matrix whose first row is $[-1, 1, 0, \cdots, 0]$, while if $\boldsymbol{x}$ is an image, $\mathcal{D}$ is the concatenation of the operators calculating the sets of vertical and horizontal transitions. The second-order difference operator $\mathcal{D}^T\mathcal{D}$ is nonnegative definite: its unique null eigenvalue corresponds to constant objects $\boldsymbol{x} \propto \mathbf{1}$.

A. The Maximal Concavity Set

If *all* transitions of $\boldsymbol{x}$ were continuous $|t_{i,j}| < q_c, \forall\, \{i,j\} \in \mathcal{C}$ (e.g., take $\boldsymbol{x} = \text{const.}$), then $\Phi_c''(\boldsymbol{x}) = 2\lambda^2 \mathcal{D}^T\mathcal{D}$. Conversely, if *all* transitions were undetermined $q_c < |t_{i,j}| \leq r_c$, then $\Phi_c''(\boldsymbol{x}) = -c\mathcal{D}^T\mathcal{D}$. Let $\mathcal{W}_c$ be the set of such *worst* objects w.r.t. maximal concavity:

$$\mathcal{W}_c = \{\boldsymbol{x} \in \mathbb{R}^M \text{ such that } \Phi_c''(\boldsymbol{x}) = -c\mathcal{D}^T\mathcal{D}\}, \qquad c < \infty. \tag{16}$$

Lemma 1—The Worst Case: Let $\mathcal{W}_c$ be as defined in (16). If $\mathcal{E}_c(\boldsymbol{x})$ is convex for any $\boldsymbol{x}$ in $\mathcal{W}_c$, then it is convex for any $\boldsymbol{x}$ in $\mathbb{R}^M$.

Proof: The second derivative of $\mathcal{E}_c(\boldsymbol{x})$ at an arbitrary point $\boldsymbol{x}$, along an arbitrary direction $\boldsymbol{v}$ is

$$\boldsymbol{v}^T\mathcal{E}_c''(\boldsymbol{x})\boldsymbol{v} = 2\boldsymbol{v}^T\mathcal{A}^T\mathcal{A}\boldsymbol{v} + \boldsymbol{v}^T\Phi_c''(\boldsymbol{x})\boldsymbol{v}. \tag{17}$$

The regularization part of (17) reads

$$\begin{aligned} \boldsymbol{v}^T\Phi_c''(\boldsymbol{x})\boldsymbol{v} &= \sum_{i\in\mathcal{S}} \sum_{j\in\mathcal{S}} v_i v_j [\Phi_c'']_{i,j} \\ &= \sum_{i\in\mathcal{S}} v_i^2 [\Phi_c'']_{i,i} + \sum_{i,j/\{i,j\}\in\mathcal{C}} v_i v_j [\Phi_c'']_{i,j} \end{aligned} \tag{18}$$

where the second sum accounts for (14). On the other hand, (15) implies

$$\begin{aligned} \sum_{i\in\mathcal{S}} v_i^2 [\Phi_c'']_{i,i} &= -\sum_{i\in\mathcal{S}} v_i^2 \sum_{j/\{i,j\}\in\mathcal{C}} [\Phi_c'']_{i,j} \\ &= -\sum_{i,j/\{i,j\}\in\mathcal{C}} \frac{(v_i^2 + v_j^2)}{2} [\Phi_c'']_{i,j} \end{aligned}$$

so that (18) also reads

$$\boldsymbol{v}^T\Phi_c''(\boldsymbol{x})\boldsymbol{v} = -\tfrac{1}{2} \sum_{i,j/\{i,j\}\in\mathcal{C}} (v_i - v_j)^2 [\Phi_c'']_{i,j}.$$

From (14), $[\Phi_c'']_{i,j}$ can only take its value from the set $\{-2\lambda^2, 0, c\}$, so

$$\boldsymbol{v}^T\Phi_c''(\boldsymbol{x})\boldsymbol{v} \geq -\frac{c}{2} \sum_{\{i,j\}\in\mathcal{C}} (v_i - v_j)^2 = -\frac{c}{2}\, \boldsymbol{v}^T\mathcal{D}^T\mathcal{D}\boldsymbol{v}$$

which provides the desired result. △

So we can find an initial convex approximation $\mathcal{E}_c(\boldsymbol{x})$ by ensuring its convexity in $\mathcal{W}_c$. However, it is important to know whether this worst situation can really occur in practice.

Lemma 2—Worst Case Occurrences: For each c *finite*, the set $\mathcal{W}_c$ in (16) is not empty.

Proof: For any objects $\boldsymbol{x}$ in $\mathcal{W}_c$, all differences $t_{i,j}$ fulfill $|t_{i,j}| \in [q_c, r_c[$. The latter interval becomes narrower as c increases, $\lim_{c\to\infty} |r_c - q_c| = 0$, but $\forall\, c$, $q_c < T < r_c$. In one dimension, a signal such as $\boldsymbol{x} = T[1, \cdots, M]^T$ remains in W_c. In two dimensions, take an image such as the symmetric Toëplitz matrix whose first row is $T[1, \cdots, M]^T$. △

B. Convexity for a Well-Posed Problem

The following convexity condition generalizes the one given in [4] for $\mathcal{A} = I$.

Theorem 2—Convexity in the Invertible Case: Let $\mu_{\min}$ be the smallest eigenvalue of $\mathcal{A}^T\mathcal{A}$ and $\nu_{\max}$ the largest eigenvalue of $\mathcal{D}^T\mathcal{D}$. Suppose $\mu_{\min} > 0$ [i.e., rank$(\mathcal{A}) = M$]. Then

$$\mathcal{E}_c(\boldsymbol{x}) \text{ is convex } \forall \boldsymbol{x} \in \mathbb{R}^M, \quad \text{if } c \leq 2\mu_{\min}/\nu_{\max}. \tag{19}$$

Proof: The proof is based upon the well known result in differential calculus that $\mathcal{E}_c(\boldsymbol{x})$—a twice differentiable function—is convex $\forall \boldsymbol{x} \in \mathbb{R}^M$ if and only if its Hessian $\mathcal{E}_c''(\boldsymbol{x})$ in (13) is nonnegative definite $\forall \boldsymbol{x} \in \mathbb{R}^M$ [22]; i.e., at each point $\boldsymbol{x}$ and along each direction $\boldsymbol{v} \neq \boldsymbol{0}$:

$$\boldsymbol{v}^T\mathcal{E}_c''(\boldsymbol{x})\boldsymbol{v} \geq 0.$$

From Lemma 1, it is sufficient to ensure convexity in $\mathcal{W}_c$. Consider the second derivative at $\boldsymbol{x} \in \mathcal{W}_c$ along an arbitrary direction $\boldsymbol{v}$. From the Rayleigh–Ritz theorem [22], $\boldsymbol{v}^T\mathcal{A}^T\mathcal{A}\boldsymbol{v} \geq \mu_{\min}\|\boldsymbol{v}\|^2$ and $\boldsymbol{v}^T\mathcal{D}^T\mathcal{D}\boldsymbol{v} \leq \nu_{\max}\|\boldsymbol{v}\|^2$, so that

$$\boldsymbol{v}^T\mathcal{E}_c''(\boldsymbol{x})\boldsymbol{v} \geq (2\mu_{\min} - c\nu_{\max})\|\boldsymbol{v}\|^2. \tag{20}$$

If $2\mu_{\min} > c\nu_{\max}$, then $\boldsymbol{v}^T\mathcal{E}_c''(\boldsymbol{x})\boldsymbol{v} > 0, \forall \boldsymbol{x} \in \mathcal{W}_c$ and $\forall \boldsymbol{v} \in \mathbb{R}^M$. △

Remark 2: Observe that $\mathcal{D}^T\mathcal{D}$ is nearly circulant and recall that the eigenvalues of a circulant matrix are the magnitudes of the discrete Fourier transform (DFT) of any row of it. Thus, $\nu_{\max} \approx 4$ for a signal and $\nu_{\max} \approx 8$ for an image in the four-nearest neighbors case [4].

Remark 3—Scale of the Operator: Inequality (19) highlights the crucial role of the *scale* of the observation operator. If the relaxed energy corresponding to $\mathcal{A}$ is convex for c_0, then the relaxed energy corresponding to $\mathcal{A}_k = k\mathcal{A}$ is convex for k^2c_0.

Remark 4—Necessary Condition: The convexity condition (19) is *sufficient*. It is also *necessary* if the maximum concavity is reachable, i.e., if equality can be reached in (20). The latter occurs whenever a direction $\boldsymbol{v}$ exists, such that

$$\|\mathcal{A}\boldsymbol{v}\|^2 = \mu_{\min}\|\boldsymbol{v}\|^2 \text{ and } \|\mathcal{D}\boldsymbol{v}\|^2 = \nu_{\max}\|\boldsymbol{v}\|^2$$

i.e., $\boldsymbol{v}$ must be simultaneously an eigenvector of $\mathcal{A}^T\mathcal{A}$ for $\mu_{\min}$, and an eigenvector of $\mathcal{D}^T\mathcal{D}$ for $\nu_{\max}$. The latter requirement is trivially satisfied when $\mathcal{A} = I$, since any vector in $\mathbb{R}^M$ is an eigenvector of I for the eigenvalue one.

C. Ill-Posed Problem

When $\mathcal{A}^T\mathcal{A}$ is singular, (19) is not applicable. The next theorem properly treats (A1) although it is a direct consequence of the previous Theorem 2.

Theorem 3—Singular Operator: If $\mathcal{A}^T\mathcal{A}$ is singular (i.e., $\mu_{\min} = 0$) and ker$(\mathcal{A}^T\mathcal{A})$ is strictly larger than Span$\{\boldsymbol{1}\}$, then $\forall c > 0$ there exists $\boldsymbol{x}$, such that $\mathcal{E}_c(\boldsymbol{x})$ is locally strictly nonconvex.

Proof: Take $\boldsymbol{v} \in \ker(\mathcal{A}^T\mathcal{A})$, $\boldsymbol{v} \notin \text{Span}\{\boldsymbol{1}\}$ and $\boldsymbol{x} \in \mathcal{W}_c$. Then $\boldsymbol{v}^T\mathcal{E}_c''(\boldsymbol{x})\boldsymbol{v} = -c\boldsymbol{v}^T\mathcal{D}^T\mathcal{D}\boldsymbol{v} < 0$, which means that $\mathcal{E}_c(\boldsymbol{x})$ is locally strictly concave in $\mathcal{W}_c$ along $\boldsymbol{v}$. △

The main consequence of this theorem is that whenever $\mathcal{A}^T\mathcal{A}$ is singular, convexity *cannot* be reached by *only* reducing c.

Remark 5—Ill-Conditioned Nonsingular Operator: When $\mathcal{A}^T\mathcal{A}$ is not singular but is still ill-conditioned, its smallest eigenvalue is $\mu_{\min} \simeq 0$. Hence, the largest c_0 satisfying (19) is $c_0 \simeq 0$; then $\mathcal{E}_{c_0}(\boldsymbol{x})$ has almost flat regions, where its minimization is extremely difficult and can even fail. Numerically, the ill-conditioned case should be treated as the singular case.

VI. GNC for an Ill-Posed Problem

Blake and Zisserman [4] stressed that (standard) GNC cannot be applied for the processing of *sparse data* ($\mathcal{A}$ is diagonal with one and zero along its diagonal, so it is singular). Instead, they recommend that sparse data first be converted to dense using a "continuous membrane" [$\alpha = \infty$ in (4)] before starting a (standard) GNC (9).

In [28] and [33] GNC was applied—with some apparent success—to the resolution of ill-posed linear inverse problems, with no explicit care of initial convexity. The regularizing function $\phi(t) = \mathbb{1}(t \neq 0)$ was relaxed according to $\phi_c(t) = 1 - \exp(-ct^2)$. It is straightforward to show that maximum concavity is $4cc^{-3/2}$, and that initial convexity occurs for $c_0 = e^{3/2}\mu_{\min}/(2\beta\nu_{\max})$ in the invertible case. According to Theorem 2, convexity can be reached even in the ill-posed case, provided that $\mathcal{A}^T\mathcal{A}$ is not singular. However, the resulting value of c is very close to zero, which provides an unacceptable nearly unregularized initial solution (e.g., Fig. 8).

On the other hand, even an "improper" c_0 could provide a unimodal initial relaxed energy since a function can be unimodal without being convex (Fig. 2). We can guess that for a given data $\boldsymbol{y}$, the concavity of $\Phi_c(\boldsymbol{x})$ reduces as c decreases toward zero and that, for some c, the relaxed energy becomes unimodal; for another data $\boldsymbol{y}$ this value would be different. Such an algorithm will be efficient for some data and it will fail for others.

In order to guarantee the uniqueness of the initial solution for $\mathcal{A}^T\mathcal{A}$ singular, we construct a *doubly* relaxed posterior energy $\mathcal{E}_{a,c}(\boldsymbol{x})$. An auxiliary convex term is appended at the earliest stage of the GNC optimization and it is relaxed to zero afterward, as follows:

$$\mathcal{E}_{a,c}(\boldsymbol{x}) = \|\mathcal{A}\boldsymbol{x} - \boldsymbol{y}\|^2 + \Phi_{a,c}(\boldsymbol{x}), \tag{21}$$

$$\Phi_{a,c}(\boldsymbol{x}) = \sum_{\{i,j\}\in\mathcal{C}} [\phi_c(t_{i,j}) + a\,t_{i,j}^2]. \tag{22}$$

From (10), piecewise concavity of $\phi_c(t)$ can be easily compensated by at^2, so that $\mathcal{E}_{a_0,c_0}(\boldsymbol{x})$ is *convex* if $a_0 \geq \frac{1}{2}c_0$. In the following, we note $\mathcal{E}_{c_k} \equiv \mathcal{E}_{0,c_k}$.

In order to bring the next stage back to standard GNC, we first relax a from a_0 to 0, $c = c_0$ remaining constant, and afterward we relax c alone:

- $c = c_0$ (fixed), for $a = a_0, \cdots, 0$
  $\check{\boldsymbol{x}}^{(a_k)} = \arg\min_{\mathcal{V}[\check{\boldsymbol{x}}^{(a_{k-1})}]} \mathcal{E}_{a_k,c_0}(\boldsymbol{x})$
- $a = 0$ (fixed), for $c = c_0, \cdots, \infty$
  $\check{\boldsymbol{x}}^{(c_k)} = \arg\min_{\mathcal{V}[\check{\boldsymbol{x}}^{(c_{k-1})}]} \mathcal{E}_{c_k}(\boldsymbol{x})$. (23)

When $\mathcal{A}$ is ill-conditioned and nonsingular, $\mathcal{E}_c(\boldsymbol{x})$ (12) is convex for c_0 close to zero. In this case, the early intermediate

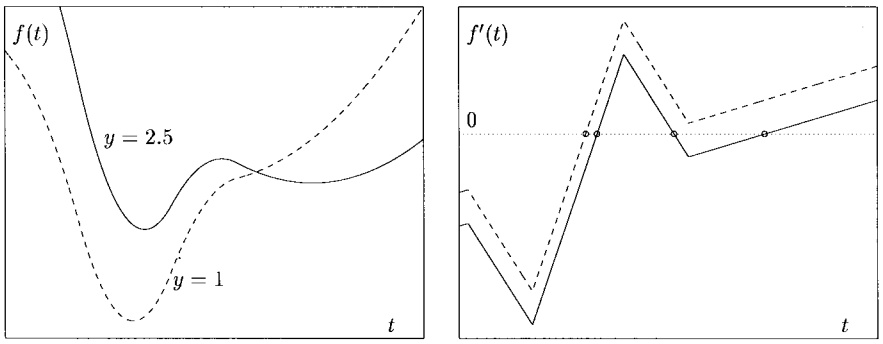

(a) (b)

Fig. 2. Nonconvex function: $f(t) = (at - y)^2 + \phi(t)$, where $a = 0.8$, $\alpha = 8$, $\lambda = 2.4$. For $y = 1$, $f(t)$ is unimodal—$f'(t) = 0$ has a unique solution—while for $y = 2.5$, $f(t)$ is bimodal, i.e., $f'(t) = 0$ admits three solutions.

solutions are very unstable while their calculation is extremely slow and precision-sensitive [$\mathcal{E}(\boldsymbol{x})$ has almost flat regions]. As long as the GNC progresses, intermediate solutions become stable and the ultimate solution is often quite satisfactory. This fact shows the practical robustness of the GNC approach. Nevertheless, the auxiliary term improves numerical efficiency: expensive minimizations over almost flat regions are avoided. Moreover, it generally leads to better reconstructions, as is shown in Section VIII.

VII. Evolution of the Solution

A. Stopping Rule

Let us examine the evolution of a GNC solution, as laid down in (23), when a and c evolve very slowly. At the beginning $c = c_0$, $a \neq 0$ and because of the quadratic term, transitions have small amplitudes. As long as a decreases, this constraint is suspended and transitions are allowed to get larger. In the same time, classification regions (11) evolve: when c increases, the undetermined zone $\pm[q_c, r_c[$ gets narrower, since $q_c \overset{\leq}{\to} T$ and $r_c \overset{\geq}{\to} T$, so the undetermined region $\pm[q_c, r_c[$ contains less and less transitions until the solution becomes entirely classified.

Definition 1—Classified Solution: An intermediate solution $\check{\boldsymbol{x}}^{(c)}$—a local minimum of $\mathcal{E}_c(\boldsymbol{x})$—is called *classified* w.r.t. c if it has no undetermined transitions, i.e., if either $|\check{t}_{i,j}| < q_c$ or $|\check{t}_{i,j}| \geq r_c, \forall \{i, j\} \in \mathcal{C}$.

The following two properties show that classification is a permanent state and that the solution gets classified for *finite* values of c (proofs are given in the Appendix).

Proposition 1—Ultimate Solution: Any classified solution $\check{\boldsymbol{x}}^{(\xi)}$ is *ultimate* in the sense that it remains unchanged if the GNC continues to run for $c > \xi$.

This yields an extremely simple *stopping rule*: if the current intermediate solution does not contain any undetermined transition, it is ultimate.

In practice, a ultimate solution $\check{\boldsymbol{x}}^{(\xi)}$ depends on $\mathcal{A}$, $\boldsymbol{y}$, (α, λ), but also on $(a_k, c_k)_{k \geq 0}$. Different relaxation sequences may provide different ultimate solutions which are local minima of $\mathcal{E}(\boldsymbol{x})$. On the other hand, there exists a *finite* value of c for which any intermediate solution is ultimate, according to the following result.

Proposition 2—Classification Bound: There exists a finite value $c = \zeta(\mathcal{A}; \lambda) < \infty$ for which *all* the minima of $\mathcal{E}_c(\boldsymbol{x})$, local and global, are classified.

Since ζ is finite, the algorithm will actually stop within a finite number of iterations. On the other hand, classification provides a convenient stopping rule which, according to practical experiments, applies far before ζ is reached, so the latter needs not be computed.

B. Scale Considerations

The whole relaxation sequence, and not just the bound ζ, must account for the observation operator and its scale. Consider (1) and its *s-scaled* copy $\boldsymbol{y}_s = s\boldsymbol{y} = \mathcal{A}_s\boldsymbol{x} + \boldsymbol{n}_s$, where $\mathcal{A}_s = s\mathcal{A}$ and $\boldsymbol{n}_s = s\boldsymbol{n}$. In order to yield the same scale-invariant solution from $\boldsymbol{y}$ and $\boldsymbol{y}_s$, the s-scaled estimator $\hat{\boldsymbol{x}}_s = \arg\min \mathcal{E}(\boldsymbol{x}; \alpha_s, \lambda_s, \boldsymbol{y}_s, \mathcal{A}_s)$ is parameterized by (α_s, λ_s). It is calculated using an s-scaled GNC relaxation with a_s, c_s: $\check{\boldsymbol{x}}^{(a_s)} = \arg\min \mathcal{E}_{a_s, c_{0s}}(\boldsymbol{x}; \alpha_s, \lambda_s, \boldsymbol{y}_s, \mathcal{A}_s)$, $\check{\boldsymbol{x}}^{(c_s)} = \arg\min \mathcal{E}_{c_s}(\boldsymbol{x}; \alpha_s, \lambda_s, \boldsymbol{y}_s, \mathcal{A}_s)$.

Theorem 4—Observation Scale: The energies $\mathcal{E}_{a,c}(\boldsymbol{x})$ and $\mathcal{E}_{a_s, c_s}(\boldsymbol{x})$ have the same local minima $[\check{\boldsymbol{x}}^{(a)}, \check{\boldsymbol{x}}^{(c)}] = [\check{\boldsymbol{x}}^{(a_s)}, \check{\boldsymbol{x}}^{(c_s)}]$ if and only if $(\lambda_s, \alpha_s) = (s\lambda, s^2\alpha)$ and $(a_s, c_s) = (s^2 a, s^2 c)$. In fact, $\mathcal{E}_{a_s, c_s}(\boldsymbol{x}) = s^2 \mathcal{E}_{a,c}(\boldsymbol{x})$ when the theorem applies.

One consequence of practical importance is that the relaxation sequence should be coarser for an amplified observation $(s > 1)$ and finer for an attenuated one $(s < 1)$. Alternatively, normalization of (1) also provides the proper scale invariance.

C. Relaxation

The initial convexified potential involved in (22) reads $\phi_{c_0}(t) + a_0 t^2$, where $a_0 \geq c_0/2$ is a sufficient condition of convexity. Clearly, choosing values of a_0 much greater than $c_0/2$ would not be judicious. On the other hand, $a_0 = c_0/2$ does not ensure that initial strict convexity be reached. A more cautious choice is to take $a_0 = c_0/1.9$, for instance.

As regards the selection of the remaining parameter c_0, the choice remains free of any mathematical constraint. It is rather a question of qualitative reasoning and practical

experience. As a matter of fact, the final solution seems to be very robust with respect to the value of c_0. Accordingly, $c_0 \approx 0.25||\mathcal{A}||_F/||I||_F = 0.25||\mathcal{A}||_F/M$ empirically appears to be sound ($||\mathcal{A}||_F$ denotes the Frobenius norm of $\mathcal{A}$). Two points are in favor of this choice. On one hand, it accounts for the scale of observation, according to Theorem 4. On the other hand, in the case $\mathcal{A} = I$, $c_0 = 0.25$ is the original value proposed by Blake and Zisserman [4]. In the general case, our choice stems from the fact that the norm of $\mathcal{A}$ is also the sum of its M singular values, so the value 0.25 will be the average quantity of the M distinct values obtained along the proper directions.

During the very early stages of the GNC, $\mathcal{E}_{a,c_0}(\boldsymbol{x})$ has only a few local minima and the form of $(a_k)_{k\geq 0}$ is not crucial; we relax a linearly in several steps. The choice of the relaxation schedule for c is guided by the following experimental observations.

1) Although a dense relaxation sequence does not guarantee attainment of the global minimum, it generally leads to a deeper minimum of $\mathcal{E}(\boldsymbol{x})$ than a coarser relaxation.
2) Large transitions are classified during the early stages of the GNC and they constitute important features of the object; details are classified later.
3) The number of classification decisions decreases with c.

These suggest to use relaxation sequences evolving slowly in the beginning and faster later. Following [4], we used an exponential relaxation sequence.

In the general context of linear ill-posed inverse problems, it seems almost impossible to infer analytical properties of the extended GNC. Instead, we provide numerical results to demonstrate its practical robustness and efficiency.

VIII. Reconstruction Results

In transmission diffraction tomography, the cross section of an object $\boldsymbol{x}$ (a cross section of the distribution of the relative propagation constant in the body) has to be recovered from some transmitted diffraction field data $\boldsymbol{y}$ [26]. In our example, a 48 $\times$ 48 [Fig. 3(c)] object reflects 12 sets of measures (projections) obtained by illumination of the object from 12 different directions in the range of $[0, 2\pi]$ radians. Under the standard Born approximation, the observation model linearly relates the 1-D Fourier transform of each set of measures to the 2-D Fourier transform of the object, calculated along a half-circle in the frequency domain [26]. The repartition of data points in the Fourier domain [Fig. 3(a)] is very irregular, so the inverse problem is ill posed, as is demonstrated by singular value decomposition (SVD) of $\mathcal{A}^T\mathcal{A}$ [Fig. 3(b)]. Noisy measurements have been simulated with signal-to-noise ratios (SNR's) of 20 and 10 dB (Fig. 4) using a normalized observation operator.

It is easy to see that both difficulties (A1) and (A2) arise in such a context. This explains why nonconvex regularization has been scarcely resorted to. We compare the reconstructions obtained with the proposed method to those yielded by different convex regularization methods. In the latter cases, the solution $\hat{\boldsymbol{x}}$ minimizes MAP energies $\mathcal{G}(\boldsymbol{x})$ of the form

$$\mathcal{G}(\boldsymbol{x}) = \|\mathcal{A}\boldsymbol{x} - \boldsymbol{y}\|^2 + \gamma \sum_{C\in\mathcal{C}} \psi(D_C\boldsymbol{x}) \qquad (24)$$

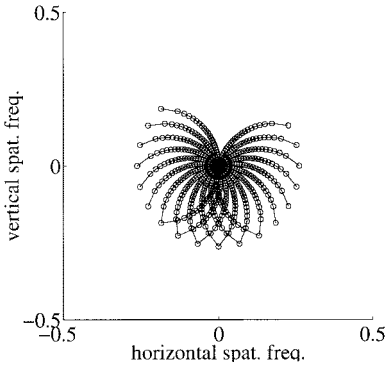

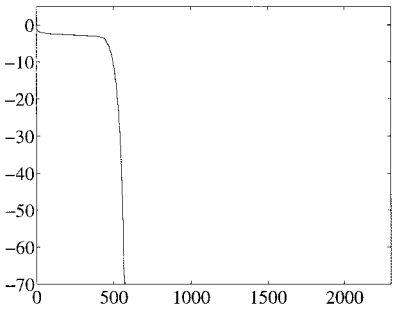

(a)

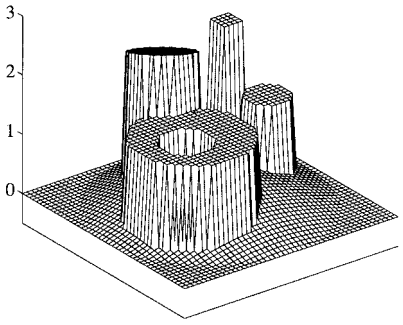

(b)

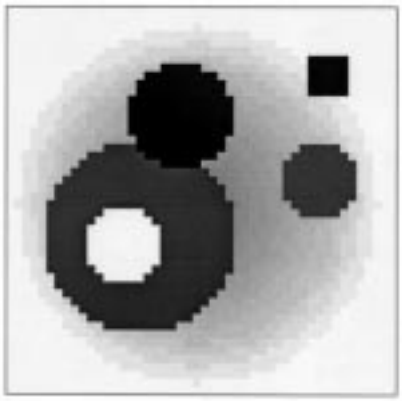

(c)

Fig. 3. (a) 12 $\times$ 48 data points in the Fourier domain. (b) Log of the SVD of $\mathcal{A}^T\mathcal{A}$. (c) Original image.

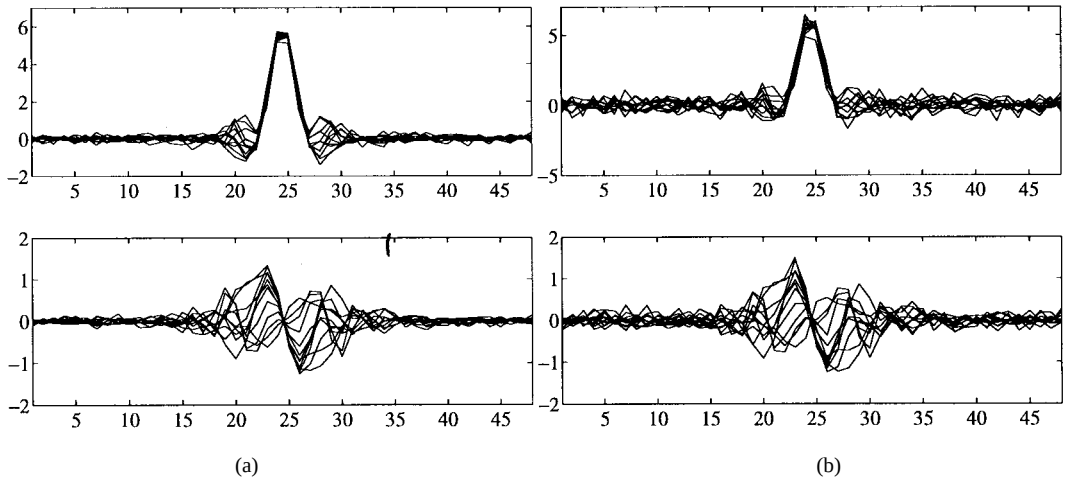

(a) (b)

Fig. 4. (a) Noisy data with 20 dB SNR: real and imaginary parts. (b) Data with 10 dB SNR: real and imaginary parts.

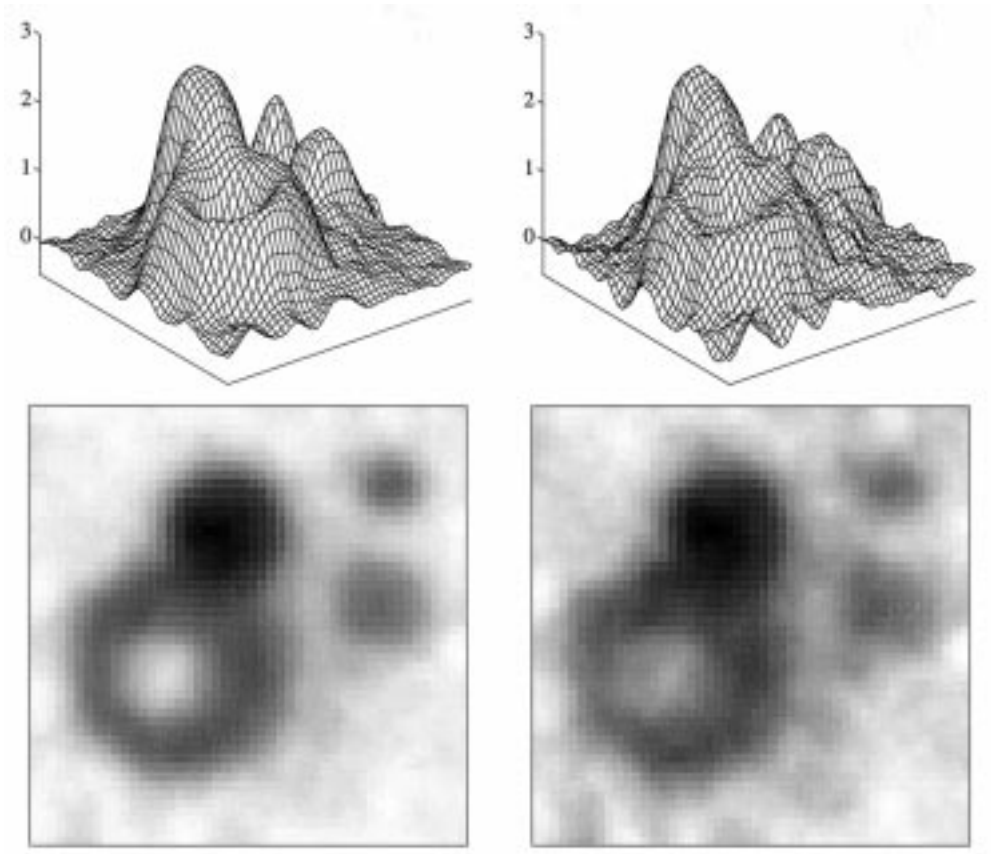

(a) (b)

Fig. 5. Reconstruction using a Gaussian MRF from the data shown in Fig. 4: (a) 20 dB SNR, $\gamma = 0.08$. (b) 10 dB SNR, $\gamma = 0.14$.

where $\psi(t)$ is *convex*. Standard descent algorithms have been used for the minimization.

Generalized Gaussians (GG's) [7] are defined by $\psi(t) = |t|^p$, where $1 < p \leq 2$ controls smoothing. The prior is a Gaussian MRF when $p = 2$ and it cancels noise at the expense of over-smoothing the edges (Fig. 5). Subsequently, GG's with $p = 1.1$ were introduced, and the 20 dB SNR and 10 dB SNR data were processed with $\gamma = 0.03$ and $\gamma = 0.07$, respectively, (Fig. 6). In the first case, the solution is stable for a smaller γ than in the second case, where transitions tend to be smooth. Sharp transitions are preserved much better with $p = 1.1$ than with $p = 2$.

The *Huber function* [23] is quadratic near the origin and affine beyond it: $\psi(t) = t^2 - (|t| - \delta)^2 \mathbb{1}(|t| \geq \delta)$. It smoothes small transitions while it adds a constant bias to large transitions. The solutions at 20 and 10 dB SNR have been

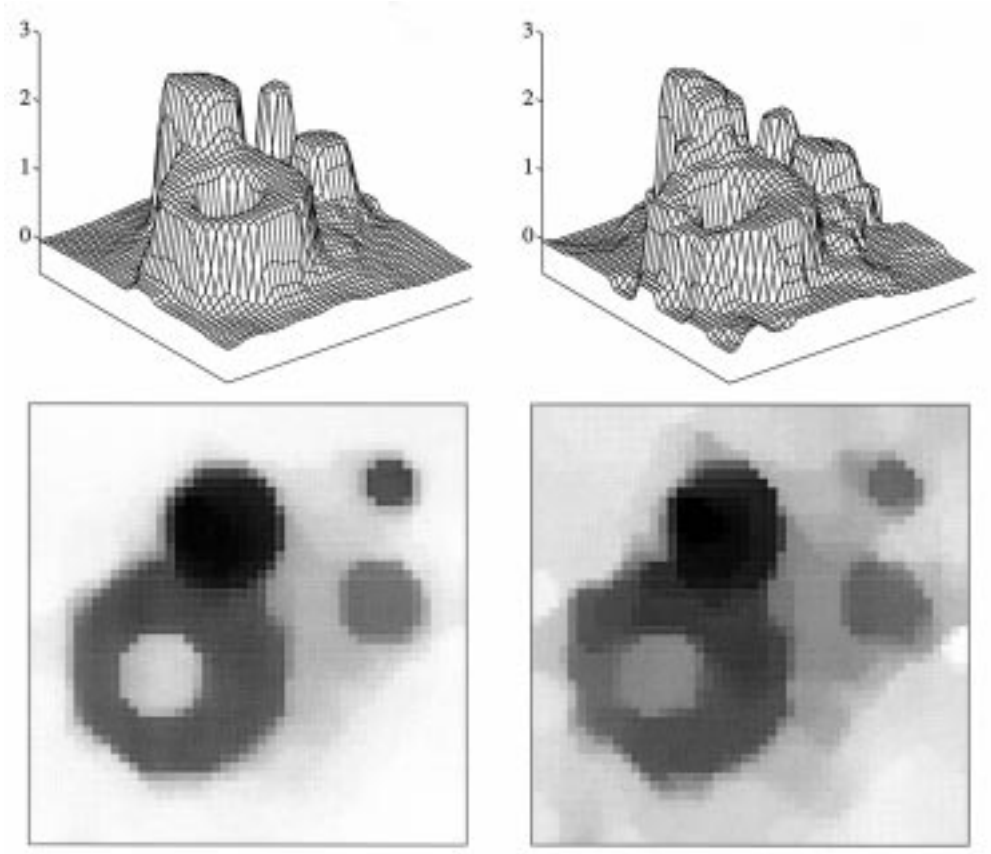

(a) (b)

Fig. 6. Reconstruction using a GG with $p = 1.1$ from the data in Fig. 4. (a) 20 dB SNR, $\gamma = 0.03$. (b) 10 dB SNR, $\gamma = 0.07$.

parameterized by $(\gamma, \delta) = (0.03, 10)$ and $(\gamma, \delta) = (0.05, 15)$, respectively (Fig. 7). Evidently, the Huber function allows the reconstruction of slightly sharper transitions than GG's with $p = 1.1$.

In contrast, the PG MRF solution (Fig. 8) provides an excellent reconstruction of both contours and smooth regions. At 20 dB SNR, data were processed using $(\alpha, \lambda) = (0.035, 0.94)$. Smooth variations in the center of the object are also well reconstructed. At 10 dB SNR, the solution was calculated for $(\alpha, \lambda) = (0.06, 1.97)$ and homogeneous regions are more strongly smoothed. In both cases, very similar solutions were obtained over a set of variations of the model parameters. The relaxation was $(a_0, a_1, a_2) = (0.13, 0.7, 0)$ and $c_k = 0.25e^{0.2k}$, $k \geq 0$.

The calculation cost of the initial solution is in fact the cost of the minimization of a convex energy. The latter is well known to be closely related to the descent algorithm being used, the conditioning of $\mathcal{A}$ and the model parameters (α, λ). The subsequent minimizations are only local, and their cost is much smaller, decreasing with the relaxation.

The initial and the ultimate solutions, obtained using *improper* GNC (without auxiliary relaxation) from the 10 dB SNR data set, are presented in Fig. 9. The initial solution corresponds to $c_0 = 10^{-3}$ and it is almost unregularized. Moreover, its calculation involves minimization over almost flat regions, which considerably increases the calculation cost. Some artifacts remain in the ultimate solution. This practically justifies our extended approach, as regards both quality and computational cost. Yet, the globally correct appearance of Fig. 8(b), except for a few aberrant pixels, points to a noticeable robustness of the GNC approach w.r.t. initialization. This solution remains clearly worse w.r.t. to the solution in Fig. 8(b). The robustness of the GNC, even improperly applied, is seen to be noticeable.

In comparison, the initial solution of the doubly relaxed GNC, obtained from the same data set with 10 dB SNR (Fig. 10), is stable, with edges preserved. This solution is similar to the reconstructions using the Huber function and GG with $p = 1.1$. The intermediate solution corresponding to $(a = 0, c_0)$ is a slightly improved version of the initial one. Recall that the ultimate solution was presented in Fig. 8(b).

IX. Concluding Remarks

MAP estimation using PG MRF's favors the reconstruction of piecewise homogeneous objects, a challenge faced in a broad set of practical situations. However, the optimal solution appears as the global minimum of a multimodal energy. Following [4] in the field of segmentation, we adopted such models and we extended the graduated nonconvexity (GNC) approach to the resolution of general linear ill-posed inverse problems.

Two specific problems were encountered, namely, i) the case of a singular or ill-conditioned general form observation operator, and ii) the case where the support of the operator is

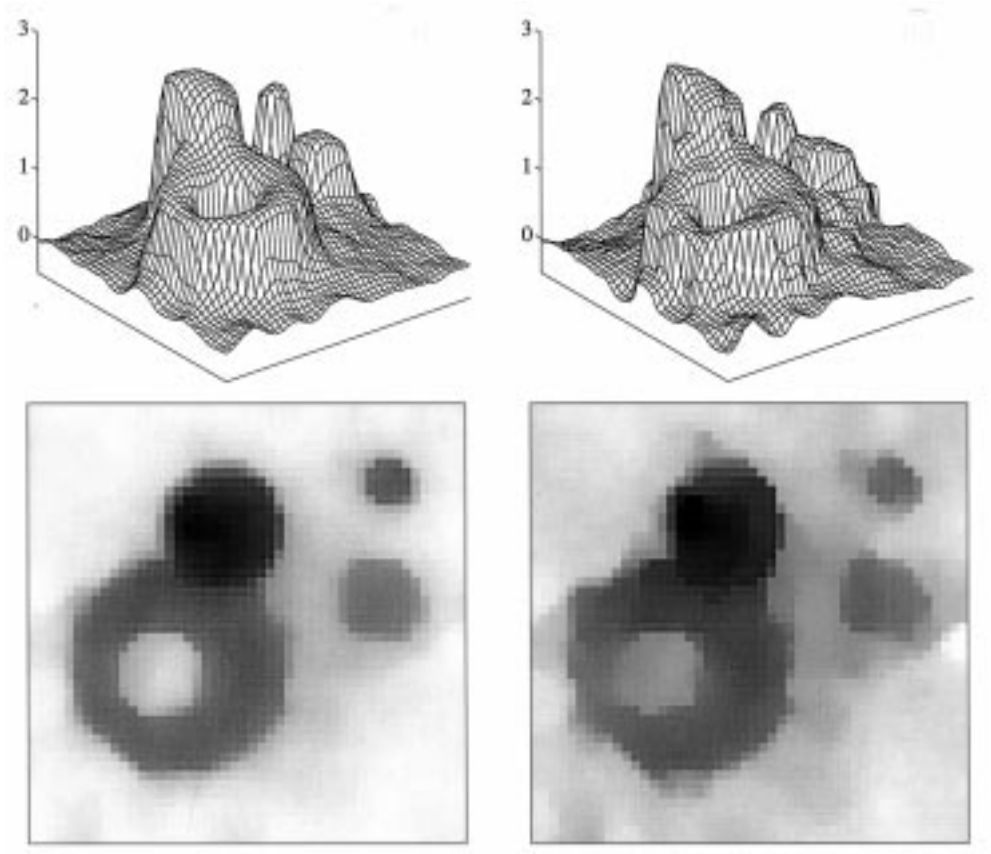

(a) (b)

Fig. 7. Reconstruction from noisy data (Fig. 4) using a regularization with a Huber function. (a) 20 dB SNR, $\gamma = 0.03, \delta = 10$. (b) 10 dB SNR, $\gamma = 0.05, \delta = 15$.

large. The latter makes the standard SA approach intractable [39]. To support this fact, a new expression of the posterior neighborhood system was provided, available for nonsymmetrical linear operators.

It was shown that the original GNC algorithm does not properly apply to ill-posed problems. We dealt with this difficulty by developing out new theoretical and practical results concerning GNC. A new modified version was proposed to cope with the ill-posed case.

Several reconstruction methods were compared in the context of synthetic noisy diffraction tomography data. The success of GNC as an edge-recovering method was apparent when compared to tractable (convex) alternatives.

APPENDIX

Proof of Theorem 1—Posterior Neighborhood: The theorem obviously holds for any prior neighborhood system ($\mathcal{N}$) and is independent of the form of the potential functions. Within this proof, a potential function on the clique C is simply noted $\phi_C(\boldsymbol{x})$. For the PG MRF, $C = \{i, j\}$ and $\phi_C(\boldsymbol{x}) = \phi(t_{i,j})$.

The posterior law reads

$$p(\boldsymbol{x}|\boldsymbol{y}) \propto \exp\left[-\sum_{C\in\mathcal{C}} \phi_C(\boldsymbol{x}) - \|\mathcal{A}\boldsymbol{x}-\boldsymbol{y}\|^2\right].$$

Let $\mathcal{C}_i$ be the set of cliques to which the pixel i contributes. The posterior neighborhood of the pixel i is composed of all the pixels j involved in the calculation of the conditional law $p(x_i|x_j,\, j \in \mathcal{S}\setminus\{i\}, \boldsymbol{y})$. It reads

$$\begin{aligned} &p(x_i|x_j,\, j\in\mathcal{S}\setminus\{i\}, \boldsymbol{y}) \\ &\quad = \frac{p(\boldsymbol{x}|\boldsymbol{y})}{p(x_j,\, j\in\mathcal{S}\setminus\{i\}|\boldsymbol{y})} \\ &\quad \propto \exp\left[-\sum_{C\in\mathcal{C}_i} \phi_C(\boldsymbol{x}) - \|\mathcal{A}\boldsymbol{x}-\boldsymbol{y}\|^2\right]. \end{aligned}$$

Furthermore, $\|\mathcal{A}\boldsymbol{x}-\boldsymbol{y}\|^2$ can be developed as a partial function of x_i

$$\begin{aligned} \|\mathcal{A}\boldsymbol{x}-\boldsymbol{y}\|^2 &= \left\|\sum_{k\in\mathcal{S}} x_k\boldsymbol{a}_k - \boldsymbol{y}\right\|^2 \\ &= \|\boldsymbol{y}\|^2 + \sum_{k\in\mathcal{S}} x_k\boldsymbol{a}_k^T(x_k\boldsymbol{a}_k - 2\boldsymbol{y}) \\ &\quad + \sum_{j\in\mathcal{S}\setminus\{i\}} x_j\boldsymbol{a}_j^T \sum_{k\in\mathcal{S}\setminus\{i,j\}} x_k\boldsymbol{a}_k \\ &\quad + x_i\boldsymbol{a}_i^T \sum_{k\in\mathcal{S}\setminus\{i\}} x_k\boldsymbol{a}_k. \end{aligned}$$

The indices of the pixels multiplying x_i in the data fidelity term are included in the last term of this sum. It shows that the pixel i interacts with any other pixel k provided that $\boldsymbol{a}_i^T\boldsymbol{a}_k \neq 0$.

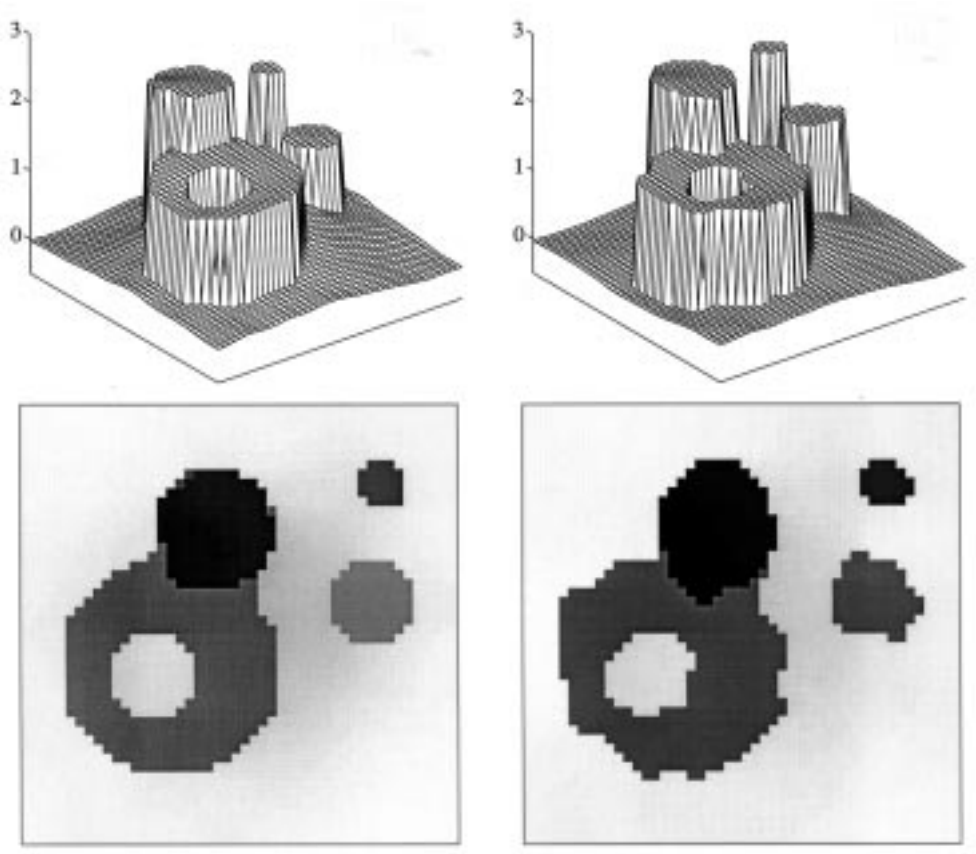

(a) (b)

Fig. 8. Reconstruction from noisy data (Fig. 4) using a PG MRF prior and the proposed GNC algorithm. (a) 20 dB SNR, $(\alpha, \lambda) = (0.035, 0.94)$. (b) 10 dB SNR, $(\alpha, \lambda) = (0.06, 1.97)$, in which case $\mathcal{E} = 117.96$.

Proof of Proposition 1—Ultimate Solution: Since $\check{\boldsymbol{x}}^{(\xi)}$ is classified, its transitions verify

$$\text{either } |\check{t}_{i,j}^{(\xi)}| < q_\xi \text{ or } |\check{t}_{i,j}^{(\xi)}| \geq r_\xi, \qquad \forall \{i, j\} \in \mathcal{C}. \tag{25}$$

According to (10), r_c decreases and q_c increases with c:

$$q_\xi < q_c \text{ and } r_\xi > r_c, \qquad \forall c > \xi. \tag{26}$$

It follows that $\check{\boldsymbol{x}}^{(\xi)}$ remains classified w.r.t. $\forall c > \xi$.

Let us show that it is also a local minimum of $\mathcal{E}_c(\boldsymbol{x})$ for $c > \xi$.

$$\mathcal{E}_c(\check{\boldsymbol{x}}^{(\xi)}) = \|\mathcal{A}\check{\boldsymbol{x}}^{(\xi)} - \boldsymbol{y}\|^2 + \sum_{\{i,j\}\in\mathcal{C}} \{[\lambda \check{t}_{i,j}^{(\xi)}]^2 \mathbb{1}[|\check{t}_{i,j}^{(\xi)}| < q_c] + \alpha \mathbb{1}[|\check{t}_{i,j}^{(\xi)}| \geq r_c]\}, \qquad c > \xi.$$

Since, from (26), $\mathbb{1}[|\check{t}_{i,j}^{(\xi)}| < q_c] = \mathbb{1}[|\check{t}_{i,j}^{(\xi)}| < q_\xi]$ for $c > \xi$, the energy $\mathcal{E}_c(\check{\boldsymbol{x}}^{(\xi)})$ is *locally independent* of c. Since $\check{\boldsymbol{x}}^{(\xi)}$ is a local minimum of $\mathcal{E}_\xi(\boldsymbol{x})$, it remains a minimum of $\mathcal{E}_c(\boldsymbol{x})$ for $c > \xi$.

Proof of Proposition 2—Classification Bound: This proof consists of the determination of ζ for signals (1-D) and for images (2-D). Indeed, ζ is a limit, independent of the data, beyond which the relaxed energy $\mathcal{E}_c(\boldsymbol{x})$ becomes strictly concave over $\pm[q_c, r_c[^M$. Since no minimum can lie in a concave region, there cannot be undetermined transitions for any $c > \zeta$. The derivation is performed in two steps. First, the energies $\mathcal{E}_{a,c}(\boldsymbol{x})$ are restated as functions of the transitions only. Then, a value of c is sought such that the relaxed energy is concave everywhere in the undetermined set $\pm[q_c, r_c[^M$.

Signals: Let $\boldsymbol{s}_A$ be the mean of the columns of $\mathcal{A}$: $\boldsymbol{s}_A = (1/M)\sum_{i=1}^M \boldsymbol{a}_i$. Let $\mathcal{D}$ be as defined in Section V-A and Q be the $M \times M$ extended invertible difference operator which transforms $\boldsymbol{x}$ into the set of transitions $\boldsymbol{b}$ and the negative sum of its elements s, as follows:

$$Q\boldsymbol{x} = \begin{bmatrix} \mathcal{D} \\ -\mathbf{1}^T \end{bmatrix}, \ \boldsymbol{x} = \begin{bmatrix} \boldsymbol{t} \\ s \end{bmatrix}, \ \boldsymbol{t} = \mathcal{D}\boldsymbol{x}, \ s = -\sum_{i=1}^M x_i.$$

The relaxed posterior energy can be restated as

$$\mathcal{E}_c(\boldsymbol{x}) = \mathcal{F}_c(\boldsymbol{t}, s) = \left\| \tilde{\mathcal{A}} \begin{bmatrix} \boldsymbol{t} \\ s \end{bmatrix} - \boldsymbol{y} \right\|^2 + \sum_{i=1}^{M-1} \phi_c(t_i),$$

$$\tilde{\mathcal{A}} = \mathcal{A}Q^{-1} = [\tilde{\boldsymbol{a}}_1, \cdots, \tilde{\boldsymbol{a}}_M],$$

$$\tilde{\boldsymbol{a}}_i = i\boldsymbol{s}_A - \sum_{j=1}^{i} \boldsymbol{a}_j, \qquad i = 1, \cdots, M-1, \ \tilde{\boldsymbol{a}}_M = -\boldsymbol{s}_A.$$

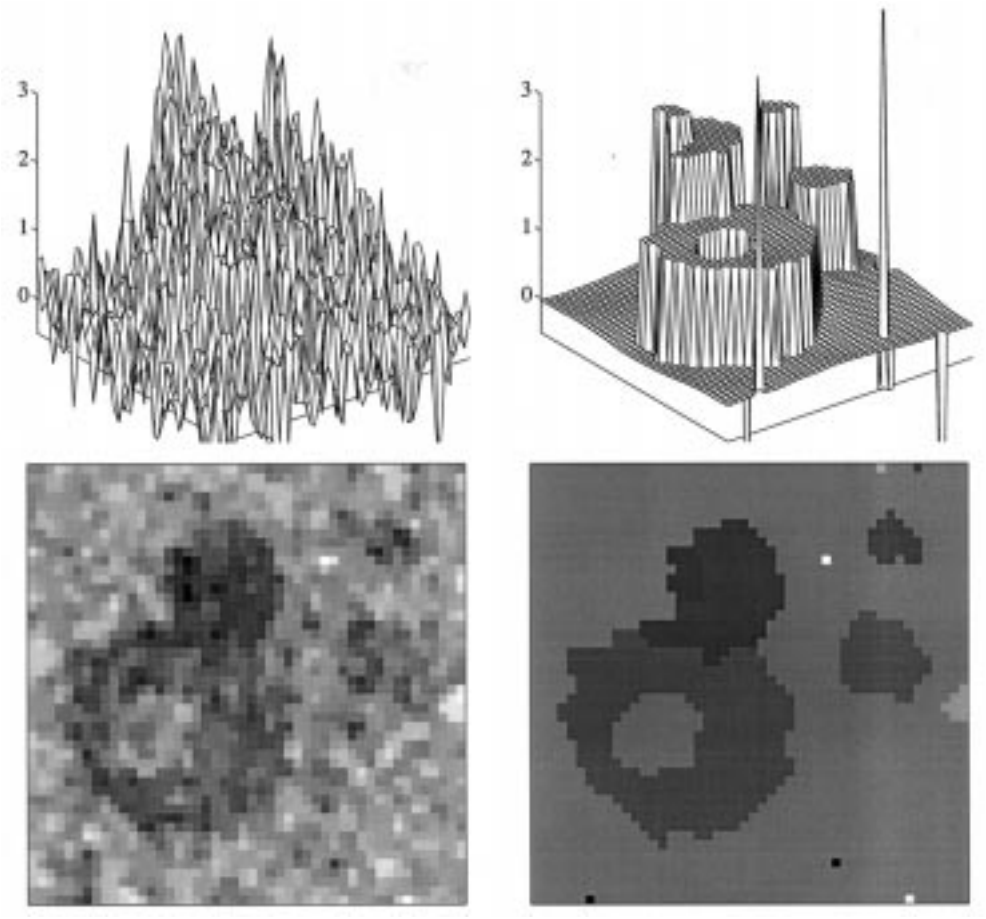

(a) (b)

Fig. 9. Reconstruction using a PG MRF prior using improper GNC (without auxiliary relaxation) in the context of Fig. 8: data in Fig. 4(b) with 10 dB SNR and model parameters $(\alpha, \lambda) = (0.06, 1.97)$. (a) The initial solution is underregularized and extremely slow to compute. (b) The ultimate solution is clearly a local minimum since its energy is $\mathcal{E} = 118.12$.

$\mathcal{F}_c(t)$, as a partial function of the ith transition, t_i, reads

$$\mathcal{F}_c(t_i;\, t_j,\, j \neq i,\, s) = t_i^2 \|\tilde{\boldsymbol{a}}_i\|^2 + t_i \mathcal{P}_i + \mathcal{Q}_i + \phi_c(t_i),$$

$$\mathcal{P}_i \equiv \mathcal{P}_i(t_j,\, j \neq i,\, s) = 2\tilde{\boldsymbol{a}}_i^T \left(\sum_{j \neq i} \tilde{\boldsymbol{a}}_j t_j + \tilde{\boldsymbol{a}}_M s - \boldsymbol{y} \right),$$

$$\mathcal{Q}_i \equiv \mathcal{Q}_i(t_j,\, j \neq i,\, s) = \left\| \sum_{j \neq i} \tilde{\boldsymbol{a}}_j t_j + \tilde{\boldsymbol{a}}_M s - \boldsymbol{y} \right\|^2 + \sum_{j \neq i} \phi_c(t_j)$$

where $\mathcal{P}_i$ and $\mathcal{Q}_i$ are independent of t_i.

At an extremum $(\check{\boldsymbol{t}},\, \check{s})$, the differential satisfies $D\mathcal{F}_c(\check{\boldsymbol{t}},\, \check{s}) = \boldsymbol{0}^T$. In particular, $\check{t}_i$ satisfies

$$\frac{\partial \mathcal{F}_c}{\partial t_i}(\check{\boldsymbol{t}},\, \check{s}) = 2\check{t}_i \|\tilde{\boldsymbol{a}}_i\|^2 + \mathcal{P}_i(\check{t}_j,\, j \neq i,\, \check{s}) + \phi_c'(\check{t}_i) = 0.$$

If $\check{t}_i$ is undetermined, $\phi_c''(\check{t}_i) = -c$ and it can be a minimum only if

$$\frac{\partial^2 \mathcal{F}_c}{\partial t_i^2}(\check{\boldsymbol{t}},\, \check{s}) = 2\|\tilde{\boldsymbol{a}}_i\|^2 - c \geq 0.$$

As a conclusion, for any i, there remains no undetermined minimum along the ith transition if $c > 2\|\tilde{\boldsymbol{a}}_i\|^2$. Then, the solution is globally classified for $c > \zeta(\mathcal{A}) = 2 \max_{1 \leq i \leq M} \|\tilde{\boldsymbol{a}}_i\|^2$.

Images: Let $\boldsymbol{x}$ be an $(m \times n)$ image, $mn = M$. Let $t^v_{i,j}$ denote a vertical transition and $t^h_{i,j}$ a horizontal transition, respectively, arranged in the vectors $\boldsymbol{t}^v$ and $\boldsymbol{t}^h$. Let $\boldsymbol{s}^v$ be the vector with the negative sums of the columns of $\boldsymbol{x}$ while $\boldsymbol{s}^h$ the vector with the negative sums of its rows. It is not difficult to determine the matrices Q^v and Q^h which furnish

$$\begin{bmatrix} \boldsymbol{t}^v \\ \boldsymbol{s}^v \end{bmatrix} = Q^v \boldsymbol{x},\, \boldsymbol{t}^v = \mathcal{D}^v \boldsymbol{x},\, \begin{bmatrix} \boldsymbol{t}^h \\ \boldsymbol{s}^h \end{bmatrix} = Q^h \boldsymbol{x},\, \boldsymbol{t}^h = \mathcal{D}^h \boldsymbol{x}.$$

The relaxed posterior energy as a function of the vertical transitions reads

$$\mathcal{F}_c(\boldsymbol{t}^v,\, \boldsymbol{s}^v) = \left\| \mathcal{A}(Q^v)^{-1} \begin{bmatrix} \boldsymbol{t}^v \\ \boldsymbol{s}^v \end{bmatrix} - \boldsymbol{y} \right\|^2 + \sum_{\{i,j\} \in \mathcal{C}^v} \phi_c(t^v_i) + \sum_{\{i,j\} \in \mathcal{C}^h} \phi_c\left(\left\{ \mathcal{D}^h (Q^v)^{-1} \begin{bmatrix} \boldsymbol{t}^v \\ \boldsymbol{s}^v \end{bmatrix} \right\}_{i,j} \right)$$

where $\mathcal{C}^v$ and $\mathcal{C}^h$ mean, respectively, the subsets of the vertical and the horizontal cliques; $[\boldsymbol{.}]_{i,j}$ denotes the $\{i, j\}$th element.

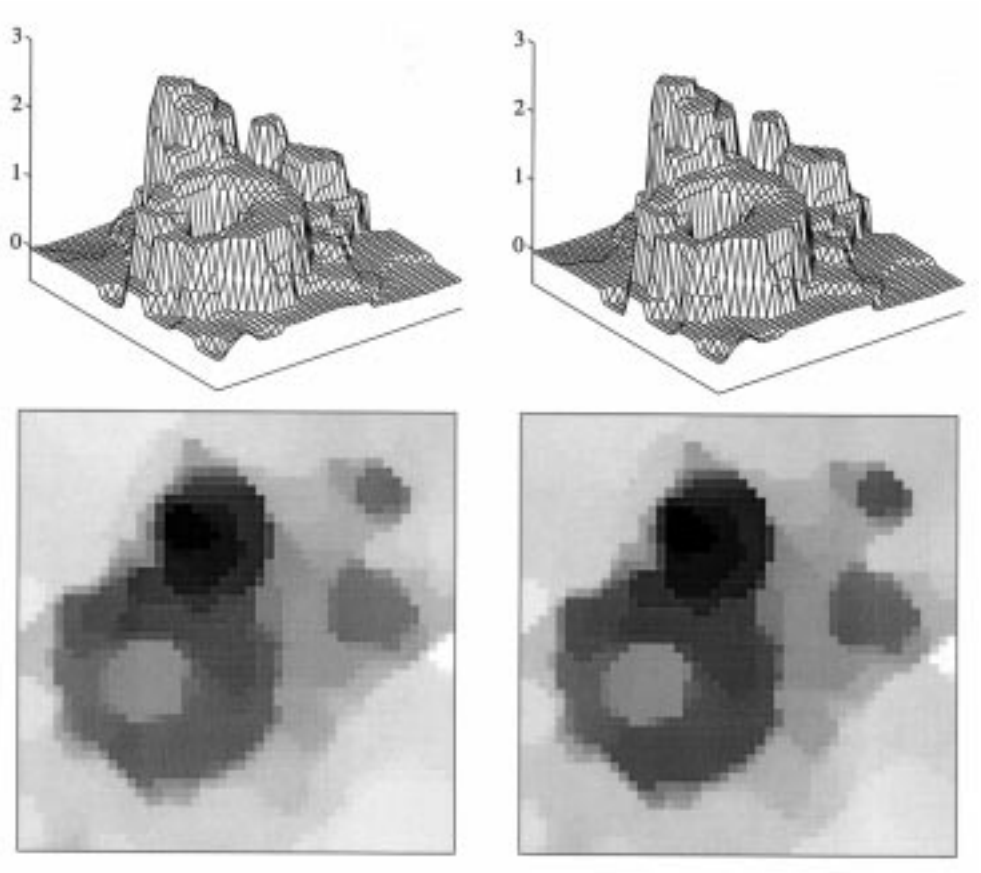

(a) (b)

Fig. 10. Initial images of the reconstruction from 10 dB SNR data (Fig. 4). (a) The first image corresponds to (a_0, c_0), where $\phi_{c_0}(t) + a_0 t^2$. It is convex and already edge preserving. (b) The intermediate solution corresponds to $(a = 0, c_0)$.

The relaxed posterior energy as a partial function of $t^v_{i,j}$ is

$$(\mathcal{F}_c)^v_{i,j} = t^{v2}_{i,j}||\tilde{\boldsymbol{a}}^v_{i,j}||^2 + t^v_{i,j}\mathcal{P}^v_{i,j} + \mathcal{Q}^v_{i,j} + \phi(t^v_{i,j}) + \sum_{l=i+1}^{m}\sum_{p=j-1}^{j}\phi\left[x_{1,p+1} - x_{1,p} + \sum_{k=1}^{l-1}(t^v_{k,p+1} - t^v_{k,p})\right]$$

where $\tilde{\boldsymbol{a}}^v_{i,j}$ is a column of $\mathcal{A}(Q^v)^{-1}$; $\mathcal{P}^v_{i,j}$ and $\mathcal{Q}^v_{i,j}$ are deduced analogously. A difference $t^v_{i,j}$ contributes to $\mathcal{F}_c$ *via* several regularization functions. A transition $\check{t}^v_{i,j}$ can be a minimum if

$$\frac{\partial^2 \mathcal{F}_c}{\partial t^2_{i,j}} = \left(2||\tilde{\boldsymbol{a}}^v_{i,j}||^2 - c + \sum \phi''_c[.]\right) > 0.$$

The upper bound of c is, in this case, $c < 2||\tilde{\boldsymbol{a}}^v_{i,j}||^2 + 4\lambda^2(m-i)$.

An equivalent form expresses $\mathcal{F}_c$ as a function of the horizontal transitions which leads to a similar bound.

Finally, all the transitions of the image are classified for

$$\zeta(\mathcal{A};\lambda) = 2\zeta_{\mathcal{A}} + 4\lambda^2(m+n),$$
$$\zeta_{\mathcal{A}} = \max[||\tilde{\boldsymbol{a}}^v_{i,j}||^2, \{i,j\} \in \mathcal{C}^v, ||\tilde{\boldsymbol{a}}^h_{i,j}||^2, \{i,j\} \in \mathcal{C}^h].$$

Proof of Theorem 4—Observation Scale: According to (21) and (22), the intermediate solutions $[\check{\boldsymbol{x}}^{(a)}, \check{\boldsymbol{x}}^{(c)}]$ and $[\check{\boldsymbol{x}}^{(a_s)}, \check{\boldsymbol{x}}^{(c_s)}]$ verify, respectively,

$$2\boldsymbol{x}^T\mathcal{A}^T\mathcal{A} + D\Phi_{a,c}(\boldsymbol{x}) = 2\boldsymbol{y}^T\mathcal{A},$$
$$s^2 2\boldsymbol{x}^T\mathcal{A}^T\mathcal{A} + D\Phi_{a_s,c_s}(\boldsymbol{x}) = s^2 2\boldsymbol{y}^T\mathcal{A}.$$

These two systems of nonlinear equations have the same set of solutions, $\forall(\mathcal{A}, \boldsymbol{y}, \alpha, \lambda, a, s)$, if and only if $D\Phi_{a_s,c_s}(\boldsymbol{x}) = s^2 D\Phi_{a,c}(\boldsymbol{x})$, which reduces to $a_s t^2 = s^2 a t^2$ and $\phi_{c_s}(t;\alpha_s,\lambda_s) = s^2\phi_c(t;\alpha,\lambda)$. The former furnishes $a_s = s^2 a$. The latter can be developed as

$$\begin{cases} (\lambda_s t)^2 = s^2(\lambda t)^2, & \text{if } |t| < q_c \text{ and } |t| < q_{c_s} \\ \alpha_s - \frac{1}{2}c_s(|t| - q_{c_s})^2, & \text{if } q_c \le |t| < r_c \text{ and} \\ \quad = s^2\left[\alpha - \frac{1}{2}c(|t| - q_c)^2\right], & \quad q_{c_s} \le |t| < r_{c_s} \\ \alpha_s = s^2\alpha, & \text{if } |t| \ge r_c \text{ and } |t| \ge r_{c_s} \end{cases}$$

which holds if and only if $\lambda_s = s\lambda$, $\alpha_s = s^2\alpha$ and $c_s = s^2 c$ (then $q_{c_s} = q_c$ and $r_{c_s} = r_c$).

ACKNOWLEDGMENT

The authors express their gratitude to F. Champagnat for his pertinent remarks about initial convexity at an early stage of this work.

REFERENCES

[1] J. E. Besag, "On the statistical analysis of dirty pictures" *J. R. Stat. Soc. B*, vol. 48, pp. 259–302, 1986.

[2] ———, "Digital image processing: Toward Bayesian image analysis," *J. Appl. Stat.*, vol. 16, pp. 395–407, 1989.

[3] G. Bilbro, W. Snyder, S. Garnier, and J. Gault, "Mean-field annealing: A formalism for constructing GNC-like algorithms," *IEEE Trans. Neural Networks*, vol. 3, pp. 131–138, Jan. 1992.

[4] A. Blake and A. Zisserman, *Visual Reconstruction.* Cambridge, MA: MIT Press, 1987.

[5] A. Blake, "Comparison of the efficiency of deterministic and stochastic algorithms for visual reconstruction," *IEEE Trans. Pattern Anal. Machine Intell.*, vol. 11, pp. 2–12, Jan. 1989.

[6] C. Bouman and B. Liu, "Segmentation of textured images using a multiple resolution approach," in *Proc. IEEE ICASSP*, Apr. 1988, pp. 1124–1127.

[7] C. Bouman and K. Sauer, "A generalized Gaussian image model for edge-preserving map estimation," *IEEE Trans. Image Processing*, vol. 2, pp. 296–310, July 1993.

[8] A. Chambolle, "Dualité Mumford-Shah/Canny-Deriche et segmentation progressive d'images," in *Actes du 14^e Colloque GRETSI*, Juan-les-Pins, France, Sept. 1993, pp. 667–669.

[9] P. Charbonnier, L. Blanc-Féraud, G. Aubert, and M. Barlaud, "Deterministic edge-preserving regularization in computed imaging," *IEEE Trans. Image Processing*, vol. 6, pp. 298–311, Feb. 1997.

[10] G. Demoment, "Image reconstruction and restoration: Overview of common estimation structure and problems," *IEEE Trans. Acoust., Speech, Signal Processing*, vol. 37, pp. 2024–2036, Dec. 1989.

[11] A. J. Devaney, "Diffraction tomography reconstruction from intensity data," *IEEE Trans. Image Processing*, vol. 1, pp. 221–228, Apr. 1992.

[12] J.-M. Dinten, "Tomographic reconstruction of axially symmetric objects: Regularization by a Markovian modelization," in *Proc. Int. Conf. on Pattern Recognition*, 1990.

[13] A. Mohammad-Djafari and G. Demoment, "Maximum entropy reconstruction in X-ray and diffraction tomography," *IEEE Trans. Med. Imag.*, vol. 7, pp. 345–354, 1988.

[14] M. Figueiredo and J. Leitao, "Simulated tearing: An algorithm for discontinuity—Preserving visual surface reconstruction," in *Proc. IEEE CVPR*, 1993, pp. 28–33.

[15] D. Geiger and F. Girosi, "Parallel and deterministic algorithms from MRF's: Surface reconstruction," *IEEE Trans. Pattern Anal. Machine Intell.*, vol. PAMI-13, pp. 401–412, May 1991.

[16] D. Geiger and A. Yuille, "A common framework for image segmentation," *Int. J. Comput. Vis.*, vol. 6, pp. 227–243, 1991.

[17] D. Geman and G. Reynolds, "Constrained restoration and recovery of discontinuities," *IEEE Trans. Pattern Anal. Machine Intell.*, vol. 14, pp. 367–383, Mar. 1992.

[18] S. Geman and D. Geman, "Stochastic relaxation, Gibbs distributions, and the Bayesian restoration of images," *IEEE Trans. Pattern Anal. Machine Intell.*, vol. PAMI-6, pp. 721–741, Nov. 1984.

[19] D. Geman and C. Yang, "Nonlinear image recovery with half-quadratic regularization," *IEEE Trans. Image Processing*, vol. 4, pp. 932–946, July 1995.

[20] P. J. Green, "Bayesian reconstructions from emission tomography data using a modified EM algorithm," *IEEE Trans. Med. Imag.*, vol. 9, pp. 84–93, Mar. 1990.

[21] E. Herman, *Image Reconstruction from Projections.* New York: Springer-Verlag, 1989.

[22] R. Horn and C. Johnson, *Matrix Analysis.* Cambridge, U.K.: Cambridge Univ. Press, 1985.

[23] P. J. Huber, *Robust Statistics.* New York: Wiley, 1981.

[24] J. Idier and Y. Goussard, "Markov modeling for Bayesian restoration of two-dimensional layered structures," *IEEE Trans. Inform. Theory*, vol. 39, pp. 1356–1373, July 1993.

[25] F. Jeng and J. Woods, "Compound Gauss–Markov random fields for image estimation," *IEEE Trans. Signal Processing*, vol. 39, pp. 683–697, Mar. 1991.

[26] A. Kak and M. Slaney, *Principles of Computerized Tomographic Imaging.* Piscataway, NJ: IEEE Press, 1987.

[27] G. Le Besnerais, J. Navaza, and G. Demoment, "Synthèse d'ouverture en radio-astronomie par maximum d'entropie sur la moyenne," in *Actes du 13^e Colloque GRETSI*, Juan-les-Pins, France, Sept. 1991, pp. 217–220.

[28] Y. Leclerc, "Constructing simple stable description for image partitioning," *Int. J. Comput. Vis.*, vol. 3, pp. 73–102, 1989.

[29] D. Mumford and J. Shah, "Boundary detection by minimizing functionals," in *Proc. IEEE ICASSP*, 1985, pp. 22–26.

[30] M. Nikolova, "Parameter selection for a Markovian signal reconstruction with edge detection," in *Proc. IEEE ICASSP*, Detroit, MI, May 1995, pp. 1804–1807.

[31] J. Ortega and W. Rheinboldt, *Iterative Solution of Nonlinear Equations in Several Variables.* New York: Academic, 1970.

[32] J. A. O'Sullivan, "Roughness penalties on finite domains," *IEEE Trans. Image Processing*, vol. 4, pp. 1258–1268, Sept. 1995.

[33] N. Saito, "Superresolution of noisy band-limited data by data adaptive regularization and its application to seismic trace inversion," in *Proc. IEEE ICASSP*, Albuquerque, NM, Apr. 1990, pp. 1237–1240.

[34] W. Snyder *et al.*, "Image relaxation: Restoration and feature extraction," *IEEE Trans. Pattern Anal. Machine Intell.*, vol. 17, pp. 620–624, June 1995.

[35] A. Tarantola, *Inverse Problem Theory: Methods for Data Fitting and Model Parameter Estimation.* Amsterdam, The Netherlands: Elsevier, 1987.

[36] D. Terzopoulos, "Regularization of inverse visual problems involving discontinuities," *IEEE Trans. Pattern Anal. Machine Intell.*, vol. PAMI-8, pp. 413–424, July 1986.

[37] A. Tikhonov and V. Arsenin, *Solutions of Ill-Posed Problems.* Washington, DC: Winston, 1977.

[38] E. Wasserstrom, "Numerical solutions by the continuation method," *SIAM Rev.*, vol. 15, pp. 89–119, Jan. 1973.

[39] C. Yang, "Efficient stochastic algorithms on locally bounded image space," *CVGIP: Graph. Models Image Process.*, vol. 55, pp. 494–506, Nov. 1993.

[40] R. Zorgati, B. Duchene, D. Lesselier, and F. Pons, "Eddy current testing of anomalies in conductive materials, part II: Quantitative imaging via deterministic and stochastic inversion techniques," *IEEE Trans. Magn.*, vol. 28, pp. 1850–1862, 1992.

Mila Nikolova received the Ph.D. degree in signal processing from the Université Paris-Sud, Paris, France, in 1995.

Currently, she is Assistant Professor (Attaché temporaire d'enseignement et de recherche) at the Université René Descartes—Paris V. Her research interests are in inverse problems and image reconstruction.

Jérôme Idier was born in France in 1966. He received the diploma degree in electrical engineering from the École Supérieure d'Électricité, Gif-sur-Yvette, France, in 1988 and the Ph.D. degree in physics from the Université de Paris-Sud, Orsay, France, in 1991.

Since 1991, he has been with the Laboratoire des Signaux et Systèmes, Centre National de la Recherche Scientifique. His major scientific interests are in probabilistic approaches to inverse problems for signal and image processing.

Ali Mohammad-Djafari (M'96) was born in Iran in 1952. He received the B.Sc. degree in electrical engineering from Polytechnique of Tehran, Iran, in 1975, the diploma degree from École Supérieure d'Électricité in 1977, and the Ph.D. degree and the Doctorat d'État, both in physical sciences, in 1981 and 1987, respectively, from the Université de Paris-Sud (UPS), Orsay, France.

He was an Associate Professor at UPS for two years. Since 1984, he has been with the Laboratoire des Signaux et Systèmes, Centre Nationale de la Recherche Scientifique. His major scientific interests are in developing new methods based on the Bayesian and maximum entropy probabilistic approaches for inverse problems in signal and image processing, especially applied to computed tomography, (X ray, PET, NMR, microwave, ultrasound, and eddy current imaging) in medical and nondestructive testing.